Impact of Microporous Layer Pore Properties on Liquid Water Transport in PEM Fuel Cells: Carbon Black Type and Perforation

Christoph Simon,[a,*,z] **Dena Kartouzian,**[a,b] **David Müller,**[a] **Florian Wilhelm,**[b] **and Hubert A. Gasteiger**[a,**]

[a]*Chair of Technical Electrochemistry, Department of Chemistry and Catalysis Research Center, Technical University of Munich, D-85748 Garching, Germany*
[b]*Centre for Solar Energy and Hydrogen Research Baden-Wuerttemberg, Division 3, Electrochemical Energy Storage and Conversion, D-89081 Ulm, Germany*

The oxygen and water transport through various microporous layers (MPLs) is investigated by fuel cell tests in a 5 cm^2 active area cell under differential-flow conditions, analyzing polarization curves, the associated high-frequency resistance, and the oxygen transport resistance extracted from limiting current density measurements. In this study, MPLs with two different carbon blacks are prepared and compared to a commercial material, all coated on the same GDL-substrate (Freudenberg); furthermore, perforated MPLs with large pores produced by a thermally decomposable polymeric pore former with a particle diameter of $\approx$30 μm are examined. The materials are characterized by mercury porosimetry, nitrogen adsorption and scanning electron microscopy. While at dry conditions ($T_{cell} = 80°C$, $RH = 70\%$, $p_{abs} = 170$ kPa) the performance of all materials is similar, at conditions of high water saturation ($T_{cell} = 50°C$, $RH = 120\%$, $p_{abs} = 300$ kPa), MPLs with larger pores or perforations exhibit a performance improvement due to a $\approx$30% reduction in oxygen transport resistance. The results indicate that liquid water is transported exclusively through these large pores, while the oxygen transport occurs in the small pores defined by the carbon black structure.

The gas diffusion layer (GDL) is a crucial component in polymer electrolyte fuel cells (PEMFC), which has to fulfil the following functions: diffusion of reactant gases from the flow fields to the catalyst layers, transport of product water in the opposite direction, conduction of electrons and reaction heat, and mechanical support of the MEA across the heterogeneous contact area between the flow field channels and lands (particularly critical under differential gas pressures between anode and cathode).[1] The GDL conventionally consists of a gas diffusion layer substrate (furtheron referred to as GDL-substrate or GDL-S) coated with a microporous layer (MPL). The GDL-substrate may be a carbon fiber paper, a non-woven carbon fiber material, or a woven carbon fiber material, usually hydrophobized by 5 wt% to 30 wt% PTFE.[1] The microporous layer is known to improve the water management at humid conditions, but also provides protection for the membrane from substrate fibers.[1–3] It consists of carbon or graphite particles and between 10 wt% and 40 wt% hydrophobic binder, characterized by pore sizes of less than 500 nm compared to the substrate pores of more than 10 μm.[1,3–5] Measurements have shown that the GDL-substrate is flooded immediately at conditions of high humidity in the absence of an MPL, initiated by water accumulation in the large pores between the fibers at the interface between the cathode electrode and the GDL-substrate, which in turn effectively blocks the diffusion of oxygen to the cathode electrode.[2,6,7] A microporous layer with its small hydrophobic pores prevents water accumulation at this critical interface between the GDL-substrate and the electrode, and also reduces the water saturation level in the GDL-substrate.[8,9]

The small pores in MPLs with a hydrophobic PTFE binder result in a high capillary pressure, which is the reason why liquid water is transported preferably via an eruptive release through cracks and larger pores.[6,10] These are either random defects in the microporous layer[11,12] or purposely designed defects.[13–18] There exist several X-ray imaging studies, which describe the liquid water transport through perforations and cracks.[14,19–21] Fuel cell tests of these types of materials have shown that specifically engineered large pores in the MPL/GDL-S can enhance the overall fuel cell performance, increase the limiting current density and accordingly reduce the oxygen transport resistance.[16,18,22]

This can be understood by considering the capillary pressure (p_c) for a hydrophobic pore as defined by the Washburn equation:[23]

$$p_c = p_L - p_V = \frac{4 \cdot \gamma_{H_2O} \cdot \cos\theta}{d_{pore}} \quad [1]$$

where γ_{H_2O} is the surface tension of water, θ is the inner contact angle of water with the pore surface, d_{pore} is the pore diameter, and p_c is the capillary pressure describing the difference between the liquid pressure (p_L) and the corresponding vapor phase pressure (p_V). The capillary pressure has to be overcome in order to fill the pore with liquid water. Since larger hydrophobic pores have a lower capillary pressure than smaller hydrophobic pores, liquid water transport should proceed predominantly through the largest pores of the MPL (under the assumption that θ is constant and $>90°$ for all pores), thereby defining the break-through pressure through the MPL.

One method to characterize the oxygen transport in the GDL-substrate and the MPL is the measurement of the limiting current density (i_{lim}) in a differentially operated fuel cell.[24–28] By variation of the oxygen concentration in the cathode feed gas, it is possible to measure the total oxygen transport resistance (R_{T,O_2}) at small and large current densities. This approach allows to characterize the oxygen transport at different operating conditions in the presence and absence of liquid water as well as the gradual saturation of the GDL.[25,26,28] Here, R_{T,O_2} is described by the sum of sequential oxygen transport resistances in the flow channels (R_{FF,O_2}), in the GDL-substrate (R_{GDL-S,O_2}), in the MPL (R_{MPL,O_2}), in the cathode electrode ($R_{cathode,O_2}$), as well as by transport resistances from other sources (R_{other,O_2}):[24]

$$R_{T,O_2} = R_{FF,O_2} + R_{GDL-S,O_2} + R_{MPL,O_2} + R_{cathode,O_2} + R_{other,O_2} \quad [2]$$

The total oxygen transport resistance R_{T,O_2} under differential-flow conditions (i.e., constant temperature, cell pressure, partial pressure, and relative humidity from cell inlet to outlet) is calculated at each dry oxygen content in the O$_2$/inert gas mixture ($x_{O_2,dry}$) by Eq. 3 based on Fick's law and Faraday's law:[26]

$$R_{T,O_2} = \frac{4 \cdot F \cdot x_{O_2,dry}}{i_{lim}} \cdot \frac{p_{abs} - p_{H_2O}}{R \cdot T_{cell}} \quad [3]$$

where T_{cell} is the cell temperature, p_{abs} is the total inlet pressure, p_{H_2O} is the vapor pressure of water at the cell temperature, F is the Faraday constant, and R is the universal gas constant. By varying the cell

Table I. MPL ink compositions and properties.

	Ink composition							MPL properties	
MPL	Carbon [g]	Triton X-100[1] [g]	Methyl cellulose [g]	DI Water [g]	PTFE[2] [ml]	PMMA [g]	Ink solids content[3] [wt%]	PTFE content[4] [wt%]	PMMA volume fraction[5] [vol%]
Li100	6.40	0.176	0.77	34.00	1.83	0	18	20	0
Li100 perforated	6.40	0.176	0.77	34.00	1.83	6.34	16	20	20
Li400	6.40	0.176	0.77	34.00	1.83	0	18	20	0
Li400 perforated	6.40	0.176	0.77	34.00	1.83	4.53	16	20	20

[1]For accurate admixing, an aqueous solution with 0.2 ml$_{\text{Triton X-100}}$/g was used.
[2]Added volume of a 58 wt% TF 5035GZ dispersion from 3 M Dyneon.
[3]Content of carbon and PTFE in the ink, defined as $m_{\text{carbon + PTFE}}/m_{\text{ink}}$.
[4]PTFE content in the MPL, assuming that only carbon and PTFE remain in the MPL after heat-treatment, and defined as $m_{\text{PTFE}}/m_{\text{carbon + PTFE}}$.
[5]Estimated PMMA volume fraction in the final MPL calculated with Equation 5 and data from Table I and Table II).

pressure, the inert gas type (N$_2$/He), and the MPL and GDL-substrate thicknesses, these resistances can be separated and furthermore divided into the relative contributions from Knudsen and molecular diffusion processes.[24,27] Limiting current density measurement, for example, have demonstrated that a GDL-substrate with a laser perforated MPL can indeed decrease the oxygen transport resistance at humid conditions.[18] The molecular diffusion contribution for each of the above transport resistances is generally described by the effective diffusion coefficient (D_{eff}) through a porous layer, which is defined by the tortuosity factor (τ) and the porosity (ϵ):

$$D_{\text{eff}} = D \cdot \frac{\tau}{\epsilon} \qquad [4]$$

where D is the molecular bulk diffusion coefficient. A commonly used estimate for τ is provided by the Bruggeman model for the diffusion around randomly distributed spheres, yielding a value of $\tau = \epsilon^{-0.5}$.[29,30] However, it has to be considered that diffusive transport in real electrochemical systems can deviate substantially from the Bruggeman prediction.[31]

The target of this study is to give novel insights into oxygen and water transport mechanisms through the MPL and to show how perforations of the MPL affect its transport properties, particularly at humid conditions. For that, we prepare MPLs with two different types of carbon black coated on a commercial GDL-substrate, further modifying the MPLs with pore-forming polymer micro-beads to produce well defined perforated MPLs. With this novel approach, we are able to engineer more defined pores compared to studies, in which salt or sucrose are used as pore-forming agent creating less defined structures.[22,32] As carbon materials, acetylene blacks are utilized, which have shown superior performance over alternative carbon materials (e.g. graphite, Vulcan XC-72).[33–37] Besides a material with typical specific surface area of 68 m^2 g^{-1}, we additionally investigate an acetylene black with a low specific surface area of 39 m^2 g^{-1}, which to our knowledge has not been investigated for MPL application so far. All materials are characterized by scanning electron microscopy (SEM), nitrogen adsorption (BET), mercury porosimetry, and thermo-gravimetric analysis. The prepared MPL/GDL-S materials are tested in a 5 cm^2 single-cell fuel cell at various conditions (temperature, relative humidity (*RH*), and pressure) with over-stoichiometric gas flow rates (i.e., under differential-flow conditions). This method allows the extraction of differential-flow polarization curves, the associated high frequency resistances (measured by AC impedance spectroscopy), and the total oxygen transport resistances, which are reported altogether for the first time for a variety of MPL materials. Our results show how the perforation of MPLs affects the oxygen transport at dry and humid conditions, and also prove that perforations in the MPL create exclusive liquid water transport pathways. Finally, we demonstrate the superior performance of our novel MPLs under fuel cell operation conditions which are considered for future fuel cell system architectures.

Experimental

MPL/GDL-substrate materials.—Two acetylene blacks Denka black Li100 (Denka; specification: spec. surface area = 68 m^2 g^{-1}, average particle size = 35 nm) and Li400 (Denka; specification: spec. surface area = 39 m^2 g^{-1}, average particle size = 48 nm) are used as framework components for the MPLs (furtheron referred to as "Li100" and "Li400" MPLs). As hydrophobic agent and binder, 58 wt% PTFE dispersion (TF 5035GZ from 3 M Dyneon) with an average particle size of 200 nm is added in order to achieve 20 wt% of PTFE in the final MPL. As solvent, deionized water (Milli-Q, 18 MΩ cm) is used. To tune the dispersibility and rheological properties of the ink, Triton X-100 (Sigma Aldrich) and methyl cellulose (Sigma-Aldrich) are admixed. For the perforated MPLs (furtheron referred to as "Li100 perforated" and "Li400 perforated"), monodisperse poly(methyl methacrylate) (PMMA) particles with a denoted average diameter of 30 μm (Soken MX-3000) are utilized as pore former polymer. All resulting inks have a volume of ≈40 ml. The composition for each MPL ink is listed in Table I including the resulting ink and MPL compositions/specifications. Here, the amount of PMMA is adjusted such that a volume fraction of PMMA (ϕ_{PMMA}) and hence, an estimated volume fraction of large pores in the final MPL of 20 vol.% for both perforated MPL types (based on Li100 and Li400) is achieved. ϕ_{PMMA} is defined according to Equation 5, where the volumes of PMMA, carbon and PTFE, calculated from the masses of the components in Table I and their material densities (ρ_{PTFE} = 2.16 g cm^{-3}, ρ_{carbon} = 1.9 g cm^{-3}, and ρ_{PMMA} = 1.19 g cm^{-3}), as well as the porosity of the carbon/PTFE fraction ϵ_{MPL} are considered. Based on the assumption that the porosities of the carbon black MPLs are the same as the porosities of the carbon/PTFE structure within the perforated MPLs, we use ϵ_{MPL} of the non-perforated Li100 and Li400 MPLs (determined from MPL weight and thickness measurements, see Equation 7 and Table II).

$$\phi_{\text{PMMA}} = \frac{V_{\text{PMMA}}}{V_{\text{PMMA}} + \frac{V_{\text{carbon}} + V_{\text{PTFE}}}{1 - \epsilon_{\text{MPL}}}}$$

$$= \frac{m_{\text{PMMA}}/\rho_{\text{PMMA}}}{m_{\text{PMMA}}/\rho_{\text{PMMA}} + \frac{m_{\text{carbon}}/\rho_{\text{carbon}} + V_{\text{PTFE}}/\rho_{\text{PTFE}}}{1 - \epsilon_{\text{MPL}}}} \qquad [5]$$

As a reference MPL/GDL-substrate material, commercially available GDL with MPL (Freudenberg) is used, which consists of a carbon black based MPL applied to a GDL-substrate, the same substrate which is used for MPL coatings in this study. Hence, when comparing different cathode GDLs, the only difference should be the MPL.

MPL preparation.—Carbon black (Li100 or Li400 type carbons), DI water, Triton X-100 and methyl cellulose are added at the specified amount (see Table I) into a 100 ml polypropylene cup. The cup is fixed into a cooling holder maintained at ≈0°C (Thinky 250AD-COOL) and mixing is conducted in an ARV-310 planetary mixer (Thinky) for 2 min at 2000 rpm and ambient pressure. Subsequently,

Table II. Carbon black powder and freestanding MPL properties. The maximum pore size is based on the dV/dlog$d$ plot in Figure 4. The MPL porosity ε_{MPL} is derived from two different methods.

MPL	BET area (powder) [m^2 g^{-1}]	BET area (MPL) [m^2 g^{-1}]	MPL porosity[1] (weight/thickness) [%]	MPL porosity (Hg intrusion)[2] [%]	Maximum pore size (Hg intrusion) [nm]
Li100	64.0	35.5	80	79 ± 1	67
Li400	37.4	19.6	73	68 ± 1	328

[1]Calculated with Eq. 7.
[2]Calculated with Eq. 9 from data in Figure 4.

the specified amount of PTFE dispersion (see Table I) is added and the ink is mixed for another 18 min at the same conditions. For inks for the perforated MPLs (Li100 perforated, Li400 perforated), PMMA particles are added at this point and intermixed for 2 min at 2000 rpm. Last, the ink is degassed under vacuum (30 kPa$_{abs}$) for 2 min at 2000 rpm in order to remove air bubbles.

The ink is coated onto GDL-substrate (Freudenberg; hydrophobically treated, ≈154 ± 10 μm thick) using a doctor blade and a stainless steel stencil with a 3.5 cm × 3.5 cm square opening and a thickness of 100 μm (for Li100 and Li400) or 75 μm (for Li100 perforated and Li400 perforated), which corresponds to a targeted MPL thickness of ≈30 μm. For freestanding MPLs used for BET analysis and mercury porosimetry, MPL inks are coated onto a smooth glass plate instead of a GDL-substrate. The coatings on the GDL-substrate or on the glass plate are immediately dried at 80°C for 30 min. Afterwards the freestanding MPLs are non-destructively removed from the glass plate by a razor blade.

In a final step the MPL/GDL-S and the freestanding MPLs are heat treated in an atmospheric oven under air in order to decompose all additive components (Triton X-100, methyl cellulose, PMMA) and to sinter the PTFE particles. The temperature is increased according to the following procedure (also see Figure 1): 10°C min^{-1} from room temperature to 200°C, 2.5°C min^{-1} from 200°C to 250°C, hold for

10 min at 250°C, 10°C min^{-1} from 250°C to 330°C, 2.5°C min^{-1} from 330°C to 380°C, hold for 30 min at 380°C, and finally cooled down to room temperature over the course of ≈2 hours.

The final thickness of the MPL is determined with a dial gauge (Mitutoyo series 543; ±3 μm accuracy) by taking the thickness of the GDLs (i.e., MPL/GDL-substrate) at five positions and subtracting the thickness of the GDL-substrate, which is measured at 8 positions around the coated area. MPLs considered for fuel cell testing have a thickness of $d_{MPL} = 30 ± 5$ μm.

$$d_{MPL} = d_{MPL/GDL-S} - d_{GDL-S} \quad [6]$$

Thermogravimetric analysis.—In order to evaluate the stability of all components during the applied MPL heat-treatment procedure, thermogravimetric analysis is performed with a TGA/DSC 1 (Mettler Toledo) on dried PTFE dispersion, methyl cellulose, Triton X-100, and PMMA particles. The applied temperature ramp is the same as for the above described MPL heat-treatment procedure (see also Figure 1). In order to simulate atmospheric conditions, the experiment is performed in 20% O$_2$ in N$_2$.

MPL porosity determination by thickness and weight.—For porosity measurements of the Li100 and Li400 MPLs, freestanding MPL samples are utilized. The MPL samples are weighed (m_{MPL}) and their thickness (d_{MPL}) is measured by a dial gauge (Mitutoyo series 543; ±3 μm accuracy) at five positions. The MPL porosity (ε_{MPL}) is determined under consideration of the material densities of PTFE ($\rho_{PTFE} = 2.16$ g cm^{-3}) and carbon black ($\rho_{carbon} = 1.9$ g cm^{-3}; manufacturer's information) and calculated MPL composition:

$$\varepsilon_{MPL} = 1 - \frac{V_{solids}}{V_{MPL}} = 1 - \frac{m_{MPL} \cdot \left(\frac{w_{carbon}}{\rho_{carbon}} + \frac{w_{PTFE}}{\rho_{PTFE}} \right)}{d_{MPL} \cdot A} \quad [7]$$

where V_{solids} is the true volume of all solids in the MPL (carbon black and PTFE), V_{MPL} is bulk volume of the MPL, m_{MPL} is the mass of the MPL, d_{MPL} is the MPL thickness, A is the coating area of 3.5 cm × 3.5 cm, and w_{carbon} and w_{PTFE} are the mass fractions in the MPL for carbon (= 0.8) and PTFE (= 0.2). The results are shown in Table II.

Mercury intrusion porosimetry.—Mercury intrusion porosimetry measurements are carried out employing two porosimeters (Pascal 140 and Pascal 440; CE Elantech, Inc. USA). GDL samples (2 samples from one batch; $m_{sample} = 210$ mg–270 mg) and freestanding MPL samples (4 samples from two different batches; $m_{sample} = 100$ mg–220 mg) are inserted in a dilatometer (sample holder). The Pascal 140 instrument is used to measure the macropore distribution by mercury intrusion at pressures ranging from vacuum to 400 kPa. On the other hand, the Pascal 440 instrument is used to measure the micropore distribution, whereby the pressure is increased in 6–19 MPa steps up to the maximum of 375 MPa while the volume increase of the mercury in the dilatometer is measured. Afterwards the pressure is decreased to vacuum in 8–35 MPa steps and the volume decrease of the mercury in the dilatometer is measured. The pore diameter (d_{pore}) is calculated using Washburn's equation

$$d_{pore} = -\frac{4 \cdot \gamma_{Hg} \cos(\theta)}{p} \quad [8]$$

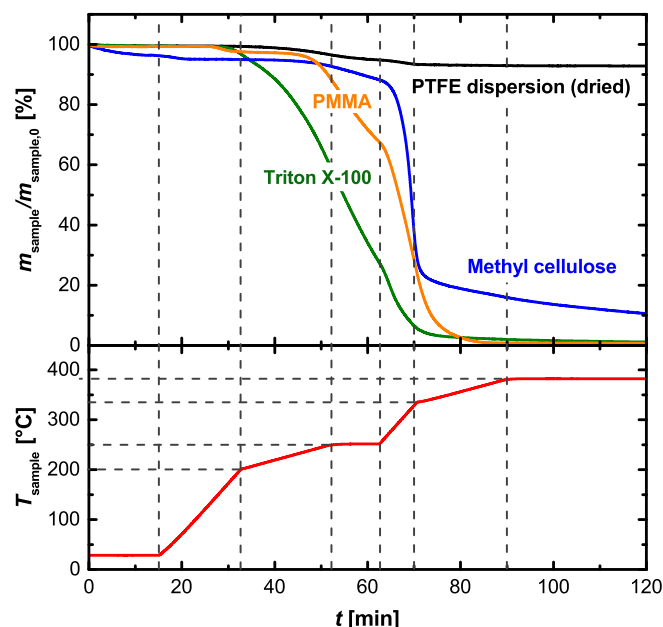**Figure 1.** Thermogravimetric analysis under synthetic air (20% O$_2$ in N$_2$) of dried PTFE dispersion (black line), Triton X-100 (green line), methyl cellulose (blue line), and 30 μm PMMA particles (orange line). Normalized sample weight $m_{sample}/m_{sample,0}$ and sample temperature T_{sample} (red line) are plotted as function of time t, whereby the temperature/time profile is identical to the heat-treatment procedure used for the preparation of GDLs and of freestanding MPLs (see Experimental).
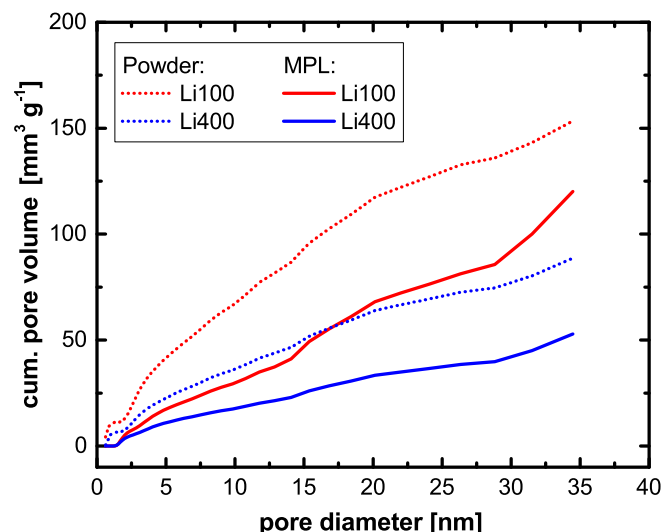
Figure 2. Cumulative pore volume as function of pore diameter measured by nitrogen sorption for Li100 and Li400 carbon powders (red/blue solid lines) and for the correspondent freestanding MPLs (red/blue dotted lines), evaluated using the QSDFT slit pore model. For better comparison of powder (carbon) and MPL (carbon and PTFE), all cum. pore volumes are normalized to the carbon weight.
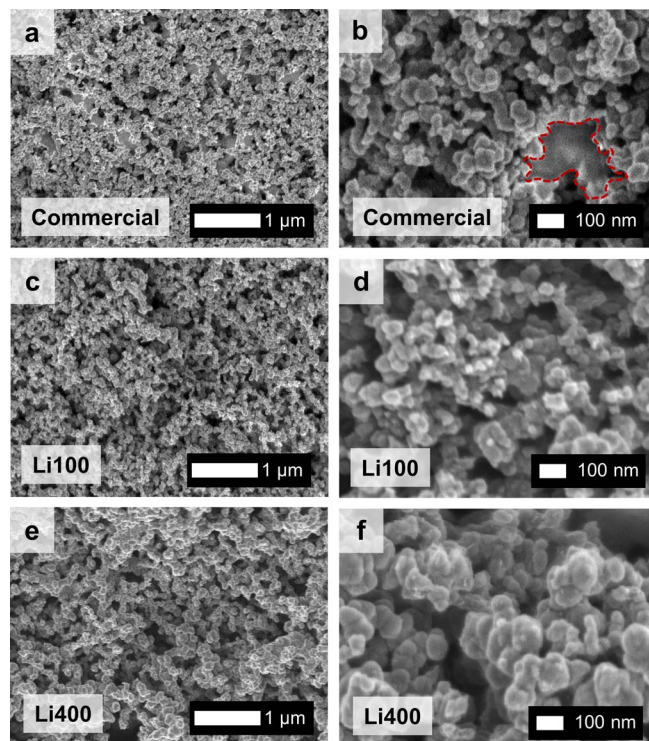

Figure 3. Scanning electron microscopy top-view images of the commercial MPL (Freudenberg) (a,b) and MPLs based on Li100 (c,d) and Li400 (e,f) carbons. Magnifications are x25,000 (a,c,e) and x100,000 (b,d,f). The red dotted marking (b) shows what we believe to be a region in which PTFE is accumulated.

where γ_{Hg} is the surface tension of mercury (0.48 N m^{-1}), θ is the inner contact angle of mercury with the pore surface (140°), and p is the mercury penetration pressure.

To exclude measurement artefacts from additional interfacial pore volume between the single sample sheets, all cumulative pore volumes are zeroed for pore diameters >10 μm for freestanding MPLs. The porosity of the MPL (ϵ_{MPL}) is then calculated from the data at maximum mercury saturation (i.e. at the maximum capillary pressure of 375 MPa) under consideration of the corrected total cumulative pore volume normalized to the sample mass v_{pore} (in units of mm$^3_{pore}$/g$_{sample}$) and the bulk MPL volume v_{MPL} (in units of mm$^3_{MPL}$/g$_{sample}$).

$$\epsilon_{MPL} = \frac{v_{pore}}{v_{MPL}} = \frac{v_{pore}}{v_{pore} + \frac{w_{carbon}}{\rho_{carbon}} + \frac{w_{PTFE}}{\rho_{PTFE}}} \quad [9]$$

Gas sorption analysis.—Pore size analysis and surface area measurements are performed on a gas sorption analyzer (Autosorb-iQ, Quantachrome, USA) using nitrogen as adsorbent at 77 K. Samples of the pure carbon powders Li100 and Li400 as well as of the stand-alone MPLs are outgassed at 250°C for 6 h under vacuum. The sample weights were chosen in order to achieve minimum absolute surface areas of >10 m^2 inside the sample vessel to attain sufficient accuracy. Adsorption and desorption isotherms with 79 points are recorded in the relative pressure range of $0.005 \leq (p/p_0) \leq 0.995$ and used to calculate surface areas with the BET method. In order to achieve comparability between powder and MPL samples, BET areas are normalized to the carbon weight (i.e., excluding PTFE weight in the case of MPLs) and are shown in Table II. Furthermore, mesoporous pore size distributions were determined using a quenched solid density functional theory (QSDFT) slit pore model (see Figure 2).[38,39]

PMMA particle size analysis.—One tip of a spatula of PMMA particles with a denoted average diameter of 30 μm (Soken MX-3000) is dispersed in water by sonication and filled together with a magnetic stirrer into the fraction cell of a laser scattering particle size analyzer (Retsch Technology, HORIBA LA-960). The measurement was evaluated with a real part refractive index of 1.49 for PMMA in water (provided in HORBIBA Control and Data Treatment Software). The resulting particle size distribution is illustrated in Figure 6.

Scanning electron microscopy.—Top-view and cross-sectional images of GDLs with and without MPL are recorded with two differ-

ent scanning electron microscopes (SEM). Top view images of MPLs w/o perforation (Li100, Li400, and the commercial MPL (Freudenberg)) are recorded in a FESEM 7500F field emission SEM (JEOL) at magnifications of x25,000 and x100,000. Secondary electron imaging is applied at an acceleration voltage between 0.8 and 1.0 kV. The images are shown in Figure 3.

All investigated GDLs are also examined in top and cross-sectional view with a JCM-6000 benchtop SEM (JCM-6000Plus, JEOL) at a magnification of x500. Cross-sectional samples are prepared by cutting the materials with a razor blade in order to create a clean cutting edge; subsequently, the materials are fixed in a cross-section sample holder together with the top-view sample. Images are taken at 5 kV acceleration voltage by a secondary electron detector and are shown in Figure 7.

Fuel cell test setup.—Fuel cell tests are realized in a 5 cm^2 active area single cell hardware (Fuel Cell Technologies) with individually designed graphite flow fields (Poco Graphite), which comprise mirror-symmetrical flow patterns for anode and cathode. The flow fields consist of 7 parallel channels with a channel and land width of 0.5 mm and a channel depth of 0.8 mm, which are arranged in one serpentine. Details are shown in Reference 40. In all experiments, a commercial anode GDL is used (Freudenberg, GDL-substrate with MPL), while the cathode GDL consists of a GDL-substrate (Freudenberg) either without or with an MPL (either a commercial MPL (Freudenberg) or MPLs developed in this study and referred to as Li100, Li400, Li100 perforated, and Li400 perforated). A Primea Mesga catalyst coated membrane (CCM, W. L. Gore & Associates A510.1/M715.18/C580.4 equipped with a sub-gasket) with catalyst loadings of 0.4 mg$_{Pt}$ cm^{-2} on the cathode and 0.1 mg$_{Pt}$ cm^{-2} on the anode is utilized as membrane electrode assembly (MEA). The square active electrode area is 5.0 cm^2, while the GDL cuttings are 5.8 cm^2 (i.e., when perfectly aligned, the GDL will extend 0.9 mm beyond the active area) in order

to assure that the GDL will always cover the active area within the errors of alignment.

A strain-controlled GDL compression of ~20% of its initial thickness is targeted in the single cell setup for a sufficient contact pressure between the layers. To realize this, PTFE coated glass fabrics (FIBERFLON GmbH & Co. KG) in the properly selected thickness are placed on the anode and cathode side as gaskets to achieve the desired compression. The initial thicknesses of the GDLs are measured at five positions and of the gaskets at eight positions by a Mitutoyo dial gauge series 543 (±3 μm accuracy, flat cylindrical tip) and the average is taken, respectively. The thicknesses of CCM and CCM gasket are measured by a SEM cross section. A detailed description of the compression calculation can be found in Reference 41.

Last, the CCM is sandwiched between the two GDLs and the flow fields. The cell endplates are tightened by eight bolts with a torque of 12 Nm in order to seal the cell. The cell is connected to a custom-designed Greenlight Innovation G60 fuel cell test station equipped with a 120 A load module (Agilent N3306A) and a potentiostat (Gamry Reference 3000).

Fuel cell test procedure.—Prior to fuel cell testing, each cell is conditioned by stepping the voltage under hydrogen (constant flows of 1390 nccm) and air (constant flow of 3320 nccm) at $T_{cell} = 80°C$, $p_{abs} = 150$ kPa, and full humidification in the following sequence: 0.6 V for 45 min, 0.95 V for 10 min, and 0.85 V for 5 min, which is repeated for ten times. Within an extensive test protocol, the following measurements are accomplished and presented in this paper. All mentioned pressures (p_{abs}) are referring to the inlet pressure in the cell, while the pressure drop is <30 kPa during all measurements (depending on operating conditions).

Potentiostatically controlled polarization curves are recorded by stepping the voltage from 0.9 V to 0.3 V (or in some cases 0.05 V) in steps of 50 mV before measuring the open circuit voltage (OCV). Each voltage is held for 10 min in controlled steady state and a 30 s average data point is recorded. After each recorded data point, an impedance spectrum is recorded from 100 kHz to 10 Hz with a perturbation voltage of 10 mV in the low noise setup of the hybrid impedance mode; the high frequency resistance (*HFR*) is determined from the high-frequency intercept of the real axis in the Nyquist representation (imaginary part vs. real part of impedance). The current-voltage curves are recorded with high constant flow rates of 2000 nccm of hydrogen and 5000 nccm of air for achieving differential flow (corresponding to H₂ and oxygen stoichiometries of s_{H_2} and s_{O_2} ≥10 at all conditions) at the following operating conditions: (i) $T_{cell} = 80°C$, $p_{abs} = 170$ kPa, $RH = 70\%$ (referred to as "dry" conditions); (ii) $T_{cell} = 80°C$, $p_{abs} = 170$ kPa, $RH = 100\%$ (referred to as "standard" conditions); (iii) $T_{cell} = 50°C$, $p_{abs} = 300$ kPa, $RH = 120\%$ ("humid" conditions); and, (iv) $T_{cell} = 80°C$, $p_{abs} = 300$ kPa, $RH = 100\%$ (referred to as "high pressure" conditions). For condition (iv), also a polarization curve in 10% O₂/N₂ is recorded in order to simulate the oxygen concentration at the stack-outlet when operating at an oxygen stoichiometry of ≈1.75 at 100% inlet *RH* (for these measurements, s_{O_2} ≥8 at all conditions).

For the measurement of the limiting current density, flow rates of 2000 nccm H₂ on the anode and 5000 nccm diluted oxygen in nitrogen in 10 different dry mole fraction ($x_{O_2,dry}$) between 0.5% and 28% on the cathode side are set. At each $x_{O_2,dry}$ the current densities corresponding to 0.30 V, 0.15 V, 0.10 V and 0.05 V are recorded by holding for 2 min in steady-state at each voltage and averaging the measured current for 15 s. The measurement conditions were the same as for the polarization curves (i), (ii), (iii), (iv) with an additional measurement at (v) $T_{cell} = 50°C$, $p_{abs} = 400$ kPa, $RH = 77\%$. The total oxygen transport resistance (R_{T,O_2}) is calculated according to Eq. 3. For all limiting current measurements recorded for this study, s_{H_2} and s_{O_2} are always ≥10 and ≥8.

Of each investigated MPL/GDL-S material two samples of the same batch are measured two times in individual cell setups. The average values and standard deviations are calculated and shown in Figure 8 (polarization curves, high frequency resistance, and oxygen transport resistance at conditions (i), (ii), (iii)), Figure 10 (summary of oxygen transport resistance), Figure 9 (oxygen transport resistance at $T_{cell} = 50°C$, $p_{abs} = 400$ kPa, $RH = 77\%$) and Figure 12 (polarization curves, high frequency resistance and oxygen transport resistance at condition (iv)).

Results

Characterization of carbon black MPLs.—In order to evaluate the thermal stability of the various MPL components during the MPL heat-treatment procedure in air, thermogravimetric analysis under air is performed following the same temperature-time profile (see lower panel of Figure 1) with all components of the MPL ink (except the carbon, which is stable under air up to ≈500°C[42]), viz., the PTFE dispersion, the Triton X-100 surfactant, the methyl cellulose thickener, and the PMMA particles used for preparing the perforated MEAs. Figure 1 shows the TGA data and the applied temperature ramp mimicking the heat-treatment procedure during the preparation of GDLs and freestanding MPLs, which is necessary to decompose undesired components in the MPL, such as emulsifiers and thickeners, and to sinter PTFE particles, which improves the overall performance.[33,34]

The dried PTFE dispersion consists of PTFE and emulsifier and is showing a weight loss of 7 wt% over the whole heat-treatment procedure, initiating at a temperature of ≈210°C and completed once the final temperature of 380°C is reached (black line in Figure 1). The observed weight loss can be explained by the loss of the surfactant, which according to the manufacturer amounts to ≈5 wt% in the dried PTFE dispersion. Thus, it can be concluded that the PTFE does not decompose to any significant fraction during the MPL heat-treatment procedure. The Triton X-100 surfactant (green line) starts to decompose after 30 min of the heat-treatment (at ≈160°C) and is completely decomposed without leaving any residue after 90 min, once a temperature of 380°C is reached; thus, the Triton X-100 surfactant added to our MPL ink will be completely removed from the MPL after its heat-treatment. This is different for the methyl cellulose thickener component added to the MPL ink (blue line). After an intial weight loss of 5 wt% after 20 min (at ≈70°C) which can be accounted to the water content in the hygroscopic substance, its rather rapid decomposition starts after 60 min (at ≈255°C), but after the end of the heat-treatment procedure (at 120 min), still 11 wt% of residue is left. Considering the composition of the MPL ink (see Table I) and that carbon and PTFE are essentially unaffected by the heat-treatment, the 11 wt% methyl cellulose residue would contribute only ≈1 wt% to the final weight of the heat treated MPL, a negligible amount which will thus not be considered in our further discussion. Finally, for the preparation of perforated MPLs, assuring the complete thermal decomposition of the PMMA pore former during temperature treatment is essential. This is indeed the case, as can be seen by the complete oxidative removal of the PMMA particles (orange line) once the temperature of 380°C is reached.

To investigate the impact of the two different carbon blacks (Li100 and Li400) on the morphology of the prepared MPLs, nitrogen sorption measurements, porosimetry results and SEM images are compared. The cumulative pore volume from nitrogen sorption measurements as function of the pore diameter for the two carbon blacks as well as for the respective MPLs is shown in Figure 2. Li100 carbon has a higher cumulative pore volume of 153 mm³ g⁻¹ between 0 nm and 35 nm compared to Li400 carbon with 88 mm³ g⁻¹. When preparing an MPL from these carbon blacks, the values decrease to 120 mm³ g⁻¹ and 52 mm³ g⁻¹, respectively, which corresponds to a pore volume reduction of 22% and 41% in the micro- and mesoporous region. This can be explained by the blocking of micro- and mesopores by the PTFE binder, which is also reflected by a decrease in BET surface area from 64.0 m² g⁻¹ to 35.5 m² g⁻¹ for Li100 and from 37.4 m² g⁻¹ to 19.6 m² g⁻¹ for Li400. As will be shown, the here observed lower cumulative pore volume of the Li400 MPL is also reflected in the pore size range between 4 nm and 50 μm by its lower cumulative pore volume in mercury porosimetry measurements (see Figure 5) and in its lower overall porosity (see Table II).
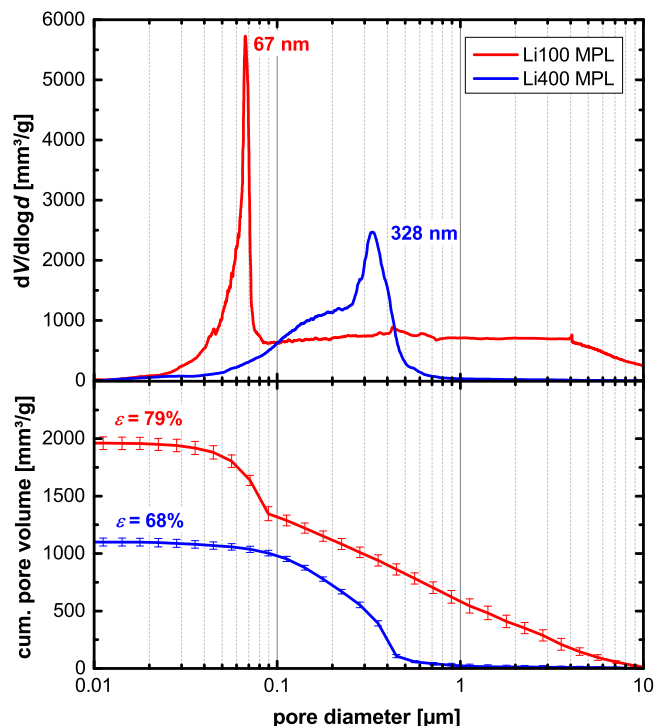
Figure 4. Cumulative pore volume (lower panel) and differential pore volume dV/dlog$d$ (upper panel) as function of pore diameter for freestanding MPLs based on Li100 (red lines) and Li400 (blue lines) carbon measured by mercury intrusion porosimetry. The lines represent the average and the error bars the standard deviation of 4 measurements for each material.

Figure 5. Cumulative pore volume (bottom) and differential pore volume dV/dlog$d$ (top) as function of pore diameter measured by mercury intrusion porosimetry for Freudenberg GDL-substrate w/o MPL (black lines) and for GDLs based on the same substrate coated with the following MPLs: commercial MPL (Freudenberg; purple lines), Li100 based MPL (red lines) and Li400 based MPL (blue lines). The lines represent the average and the error bars the standard deviation of 2 measurements for each material.

Next, we examine the morphology of the commercial MPL (MPL/GDL-S from Freudenberg) and compare it to our experimental MPLs (Li100 and Li400 MPLs) using SEM. Figure 3 shows SEM top-view images of these MPLs with magnifications of 25,000 and 100,000, where the porous structure of the MPL, the carbon black primary particles, and the agglomerate structure can be discerned. Here it should be noted that the non-conductive PTFE component in the MPL can hardly be distinguished in the images. However, in the case of the commercial MPL (Figures 3a and 3b) we can see agglomerates on the order of ≈100–300 nm in diameter (see red dotted marking in Figure 3b) which are characterized by a uniform surface significantly different from carbon black particles. Hence, they can be attributed to contaminations, residues from additives, or to accumulated, non-dispersed PTFE, which is either available as homogeneous particle or is covering a carbon black agglomerate. In the case of the Li100 and Li400 based MPLs, such spots are not observed. Since the PTFE particles in the dispersion used in this study have a mean particle size of 200 nm, this observation is an indication that the PTFE in our MPLs is dispersed as a thin film or as substantially smaller particles. This would create more homogeneously hydrophobic surfaces throughout and across the whole MPL.

With respect to the primary particle size of the different carbons, the SEM images of the commercial and the Li100 MPL (Figures 3b and 3d) reveal similar primary particle sizes, whereas clearly larger primary particle sizes are observed for the Li400 carbon in the Li400 MPL (Figure 3f). The larger primary particle size of the Li400 carbon compared to the Li100 carbon as observed in these SEM images is consistent with the manufacturer's specifications (48 nm for Li400 and 35 nm for Li100) and also with the ≈1.5-fold lower BET area of the Li400 carbon. A comparison of Figures 3b and 3d with Figure 3f also indicates qualitatively that the average macropore size in the commercial and the Li100 MPL is substantially smaller than that of the Li400 MPL.

A more quantitative description of the macropore size distribution of the Li100 and Li400 based MPLs can be obtained by mercury
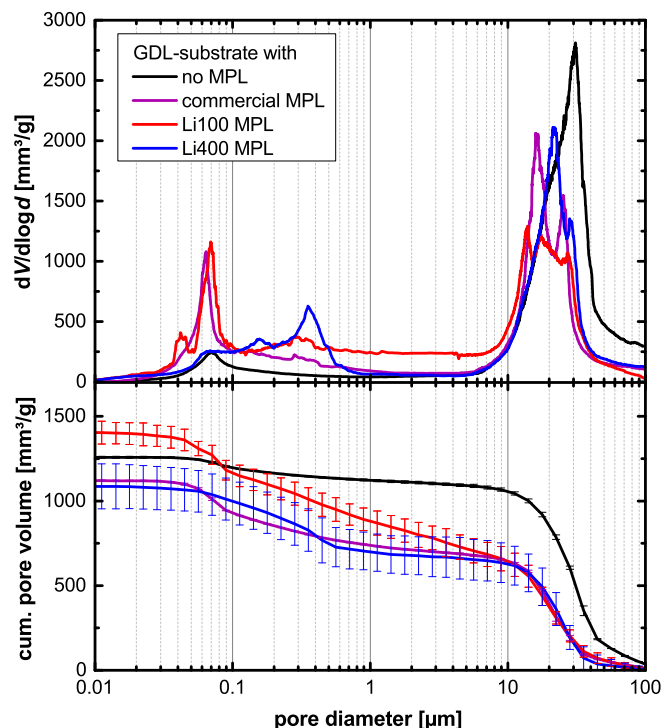
porosimetry of the freestanding Li100 and Li400 MPLs, which is illustrated in Figure 4. The pore sizes of the Li100 MPL show a very broad distribution between ≈30 nm and ≈10 μm, with a maximum in the dV/dlog$d$ plot at 67 nm (upper panel, red line). As already indicated in the above SEM analysis, this is much smaller than the pore size distribution maximum of 328 nm observed for the Li400 MPL (blue line). The reason for the substantial pore volume in the >1 μm range of the freestanding Li100 MPL (ca. 29%, see lower panel of Figure 4) is not yet clear, but it is also observed for the Li100 MPL coated on the GDL-substrate (Figure 5) and may be due to some cracks in the layer (see later discussion on SEM cross-sections). The total cumulative pore volumes of the freestanding MPLs (lower panel) significantly differ from each other, with the Li100 MPL exhibiting 1101 ± 36 mm^3 g^{-1} and the Li400 MPL 1969 ± 56 mm^3 g^{-1}; based on Equation 9, this corresponds to overall MPL porosities (ε_{MPL}) of 79% (Li100 MPL) and of 68% (Li400 MPL), suggesting a higher packing density for the Li400 carbon within the MPL.

The results of the porosity analysis are listed in Table II. The porosities determined by the two different methods (weight and thickness measurements or Hg intrusion on freestanding MPLs) are in quite excellent agreement and clearly show that the packing density of the Li400 carbon in the MPL is higher than that of the Li100 carbon. In summary, the Li400 MPL composed of the carbon with the larger primary particles has a maximum in the pore size distribution which is at a substantially larger diameter (consistent with the visual observations in Figure 3), but exhibits smaller porosity compared to the Li100 MPL.

In order to investigate the interaction between MPL and GDL-substrate and to compare MPL/GDL-substrate samples with the commercial GDL-substrate and the commercial MPL/GDL-substrate, Figure 5 shows the Hg intrusion porosimetry results for the substrate and the respective MPLs including the commercial MPL coated on the same substrate. The GDL-substrate itself (black curve in Figure 5)
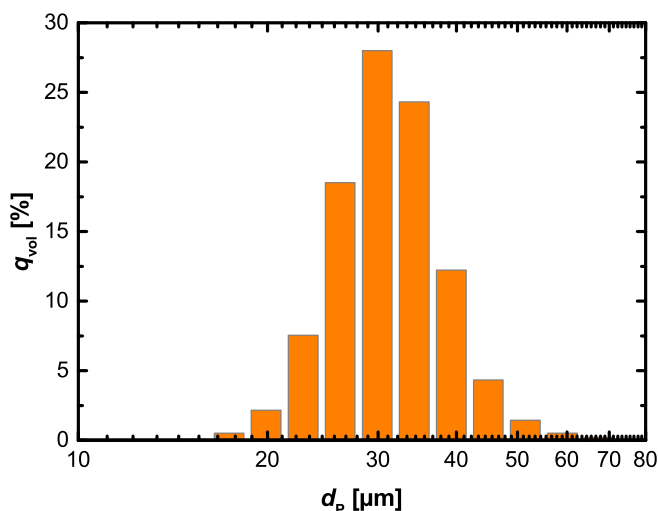
Figure 6. Volumetric particle size distribution of Soken PMMA 30 μm particles measured by laser scattering in aqueous dispersion (note that the particle diameter is plotted on a logarithmic scale).

has a peak maximum at 30.5 μm (upper panel) and ≈89% of the pore volume in the >1 μm range (lower panel). A small peak in the pore size distribution is visible at a pore diameter of ≈70 nm; this, we believe, originates from carbon particles which are a constituent of the GDL-substrate and which are also visible in the SEM images in Figures 7a and 7b. The GDL-substrate pore size distributions (>10 μm) of the GDL-substrate coated with MPLs (magenta, red, and blue lines) all show a slight shift toward smaller pore sizes compared to the virgin substrate, suggesting that large pores close to the substrate surface are partially filled with the MPL ink during coating, therby leading to a reduction of pore volume in the large pore range. The Hg porosimetry data of the GDL-substrate with the different MPLs also allows a comparison of the Li100 and Li400 based MPLs with the commercial reference MPL, showing that the pore size maximum of the commercial MPL (≈64 nm) is essentially identical to that of the Li100 MPL on the GDL-substrate (≈69 nm) and that of the freestanding Li100 MPL (≈67 nm; see Figure 4), with both being substantially smaller than the pore size maximum of the Li400 MPL on the GDL-substrate (≈353 nm) and of the freestanding Li400 MPL (≈328 nm; see Figure 4). In the ≈0.6-6 μm region where there is no contribution from the GDL-substrate, the pore volume of the GDL-substrate supported Li100 MPL is quite substantial, while it is insignificant for the GDL-substrate supported Li400 MPL, essentially identical with the data for the freestanding MPLs (Figure 4). In this same pore size region, the commercial MPL resembles the behavior of the Li400 MPLs, also not exhibiting any significant pore volume. One possible reason for the presence/absence of pore volume in the ≈0.6-6 μm region can be gleaned from the inspection of SEM cross-sectional images and will be discussed later.

Characterization of perforated MPLs.—Perforations in the Li100 and Li400 MPLs are obtained by mixing the MPL ink with PMMA particles serving as pore former, which will be completely decomposed during the MPL heat-treatment (after 90 min at 380°C, see Figure 1). Hence, the final MPL would be expected to contain holes in the size of the PMMA particles. The volumetric particle size distribution of the PMMA powder is shown in Figure 6. In the logarithmic plot an approximate normal distribution is observed with a maximum at 30 μm, which is also the mean particle diameter and in agreement with the product specifications. The chosen particle diameter of 30 μm is identical with the targeted MPL thickness, with the expectation that after the thermal decomposition of the PMMA particles large pores through the entire thickness of the MPL be formed, which would provide pathways for liquid water transport through the whole MPL.

To investigate the MPL/GDL-substrate structures in the μm-range (i.e., in the range of the targeted MPL perforations), Figure 7 is illustrating SEM images at 500x magnification in top-view (MPL side) and cross-sectional view of all prepared and tested GDLs. All considered MPLs are coated on substrate, which is shown in Figures 7a and 7b. The non-woven fabric is 154 ± 4 μm thick and consists of ≈10 μm thick carbon fibers (estimated from SEM images), which are disorderly arranged. At the boundary points between the fibers, an aggregation of material is observed which must originate from the production process of the substrate (remainings of a pyrolized resin binder) and/or from a subsequent hydrophobic treatment including a carbon component in order to prevent water adhesion in the substrate (the latter would explain the observed pore size distribution maximum at ≈70 nm of the GDL-substrate in Figure 5). Figures 7c–7l illustrate the coated MPLs on GDL-substrate in top-view and cross-sectional view (MPL on top, GDL-substrate on the bottom).

The commercial MPL (Figures 7c and 7d) reveals small holes of a few μm in diameter on the surface, which could originate from air bubbles. Other than that, the surface is crack-free, which is also observed in the cross-sectional view. The interface between the MPL and the GDL-substrate is rather sharp, suggesting that minimal penetration of the MPL ink into the GDL-substrate during the coating process. The Li100 (Figures 7e and 7f) and Li400 (Figures 7i and 7j) MPLs also exhibit almost faultless MPL top surfaces, while the cross-sections reveal the presence of cracks which partially penetrate through the MPL (mostly originating at the MPL/GDL-substrate interface). This is particularly pronounced for the Li100 MPL, which might be the origin of its substantial pore volume in the ≈0.6-6 μm range observed by mercury porosimetry (see Figure 5). Contrary to the commercial MPL/GDL-substrate, a distinct intrusion of the MPL ink into the substrate is observed for the Li100 and Li400 samples, clearly discernable by the MPL-surrounded fibers.

The perforated MPLs based on Li100 (Figures 7g and 7h) and Li400 (Figures 7k and 7l) feature several μm wide cracks and holes on the surface and across the thickness of the MPL. Some of the pores invade deeply into the material and penetrate through the entire MPL; however, even though PMMA particles with a mean diameter of 30 μm are utilized, we were not able to see ≈30 μm pores in the SEM images. Nevertheless, as intended by our MPL design strategy, μm large pathways across the MPL have indeed been accomplished, and it remains to be seen whether they will positively affect the transport of liquid water. However, compared to non-perforated MPLs, the pore former clearly creates a very uneven surface (Figures 7g and 7k). Although the PMMA content is supposed to form 20 vol.% of additional perforation pore volume which would result in a porosity of 86% for the perforated Li100 MPL (based on $\varepsilon_{MPL} = 79\%$ for the Li100 MPL from Table II) and of 77% for the perforated Li400 MPL (based on $\varepsilon_{MPL} = 68\%$ for the Li400 MPL from Table II), it might be the case that the pore volume is larger than expected due to the formation of additional cracks caused by tension around the PMMA particle during the drying procedure. Unfortunately, based on the available methods it is experimentally not possible to determine the porosity of the perforated MPL, because the perforated MPLs are too brittle and uneven to measure their accurate thickness or to perform mercury porosimetry. As well, the MPLs coated on the GDL-substrate have similar pore sizes as the substrate itself which would make a deconvolution between substrate pores and large MPL pores challenging.

Fuel cell tests.—Results from the fuel cell tests with the different cathode MPLs are shown in Figure 8. Differential-flow polarization curves (top) at dry (a), standard (b) and humid (c) conditions together with the associated *HFR* values (middle) as well as the total oxygen transport resistances R_{T,O_2} (bottom) are shown. The dry conditions (a) at $T_{cell} = 80°C$, $RH = 70\%$ and $p_{abs} = 170$ kPa represent an operating condition, in which no liquid water is expected to be present, neither in the MPL/GDL-substrate due to the low relative humidity and the high operating temperature, nor in the flow field channels due to high flow rates. On the contrary, the humid conditions (c) at low operating
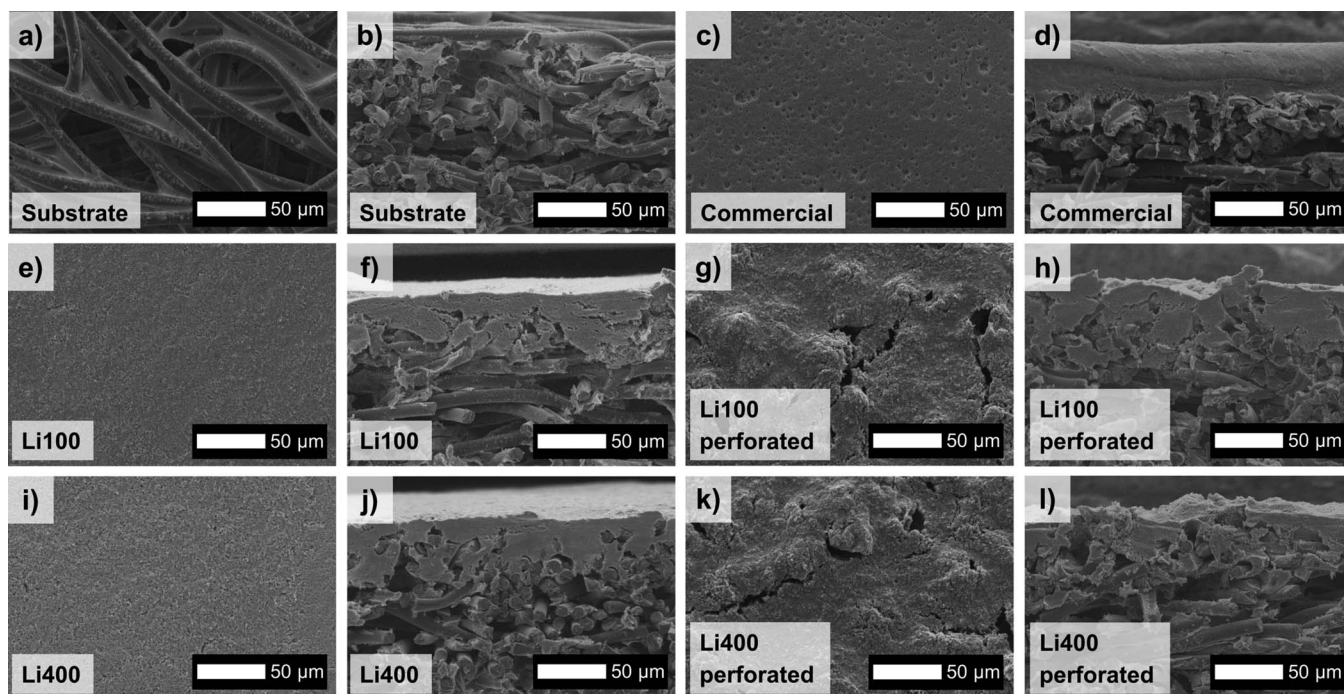
Figure 7. Scanning electron microscopy images for MPLs in top-view (a,c,e,g,i,k) and cross-sectional view (c,d,f,h,j,l) for Freudenberg GDL-substrate w/o MPL (a,b) and the following MPLs coated on the same substrate: commercial MPL (Freudenberg) (c,d), Li100 based MPL (e,f), perforated Li100 based MPL (g,h), Li400 based MPL (i,j), perforated Li400 based MPL (k,l). Magnification for all images is x500.

temperature of $T_{cell} = 50°C$ (small saturation vapor pressure), oversaturated gas fluxes with $RH = 120\%$ (fully saturated gas phase) and a high pressure of $p_{abs} = 300$ kPa (decreased diffusivity of water vapor in the gas phase) facilitate the condensation of liquid water inside the MPL/GDL-substrate. Finally, the standard conditions (b) represent a typical operating state of a PEM fuel cell at $T_{cell} = 80°C$, $RH = 100\%$, $p_{abs} = 170$ kPa. Although fully saturated gas streams are fed into the fuel cell at these operating conditions, we will show that our data suggest that liquid water does not play a major role here in terms of oxygen transport.

The differential-flow polarization curves at dry and standard conditions show a very similar trend. The region from 0 A cm^{-2} to ≈ 2.5 A cm^{-2} is dominated by kinetic and ohmic resistances, whereas from ≈ 2.5 A cm^{-2} on mass transport losses become significant, which is indicated by the change from a nearly linear voltage loss with current density between ≈ 1.0 A cm^{-2} and 2.5 A cm^{-2} to a more rapid decrease of cell voltage. At a cell voltage of 0.6 V, the performance curves for all materials except the Li100 MPL with perforation reach ≈ 1.7 A cm^{-2} at dry and ≈ 2.2 A cm^{-2} at standard conditions. The smaller current density at dry conditions can be explained with the high frequency resistance, which is 50% higher at dry conditions (≈ 45 mΩ cm^2) than at standard conditions (≈ 30 mΩ cm^2), showing that the lower RH of 70% leads to an increased membrane resistance and a concomitantly higher proton conduction resistance in the electrodes. The significant increase of the HFR at current densities exceeding ≈ 3 A cm^{-2} under both dry and standard conditions indicates a reduced local RH (at the electrode and the membrane) due to a growing temperature gradient between the flow field and the MEA. The polarization curve of the Li100 MPL with perforation, however performs worse than the other GDLs for both conditions at 80°C. For this GDL material, the HFR is ≈ 10 mΩ cm^2 higher than for the others, which would predict a voltage difference of 20 mV at 2.0 A cm^{-2}. This value is in reasonable agreement with the difference of the polarization curves. The most likely reason for this difference in HFR is a higher contact resistance caused by an uneven contact area by the perforation (see Figure 7g), particularly since the differences are the same for both 70% and 100%

RH conditions. Why this is not observed for the Li400 MPL despite its similar surface morphology (see Figure 7k) is unclear at this point.

In contrast to the dry and standard conditions, significant differences in the polarization curves are measured at humid conditions. At 0.6 V, the performance varies between 1.8 A cm^{-2} and 2.4 A cm^{-2} in the following ascending order: commercial MPL, no MPL, Li100 MPL, Li400 MPL, Li100 MPL with perforation and Li400 MPL with perforation. This trend becomes even more pronounced at lower voltages, where mass transport limitations become relevant. Under these conditions, the HFR for the perforated Li100 MPL is now only slightly higher than that for the other GDLs (by ≈ 3-5 mΩ cm^2), which might be due to a higher compressive force induced by membrane swelling under over-humidified conditions, which in turn would reduce the effect from contact resistance differences between the MPL surface and the electrode. Clearly, however, the performance differences cannot be due to ohmic resistances and must be caused by differences in the oxygen transport resistance R_{T,O_2}.

At current densities below ≈ 1.5 A cm^{-2}, the total oxygen transport resistance is almost identical for dry and standard conditions (lower panels in Figures 8a and 8b) and also varies very little with the type of GDL: the substrate without MPL has the smallest R_{T,O_2} (as expected in the absence of liquid water[41]), followed in increasing order by the GDLs with perforated MPLs, with the Li100/Li400 MPLs, and with the commercial MPL. On the other hand, large differences in R_{T,O_2} are observed under humid conditions (lower panel in Figure 8c), with the highest value observed for the substrate without MPL. This can be attributed to water condensation at interface between the GDL-substrate and the cathode catalyst layer, which hinders oxygen diffusion.[2] Clearly, while an MPL is not necessary and actually adds oxygen transport resistance under dry conditions, it prevents the accumulation of water at the electrode/GDL interface under humid conditions and thereby reduces the oxygen transport resistance. Hence, all MPLs significantly reduce R_{T,O_2} in the following order beginning with the highest R_{T,O_2}: commercial MPL, Li100 MPL, Li400 MPL, Li100 perforated MPL and Li400 perforated MPL, while the latter two exhibit almost the same resistance. In general, it has to be
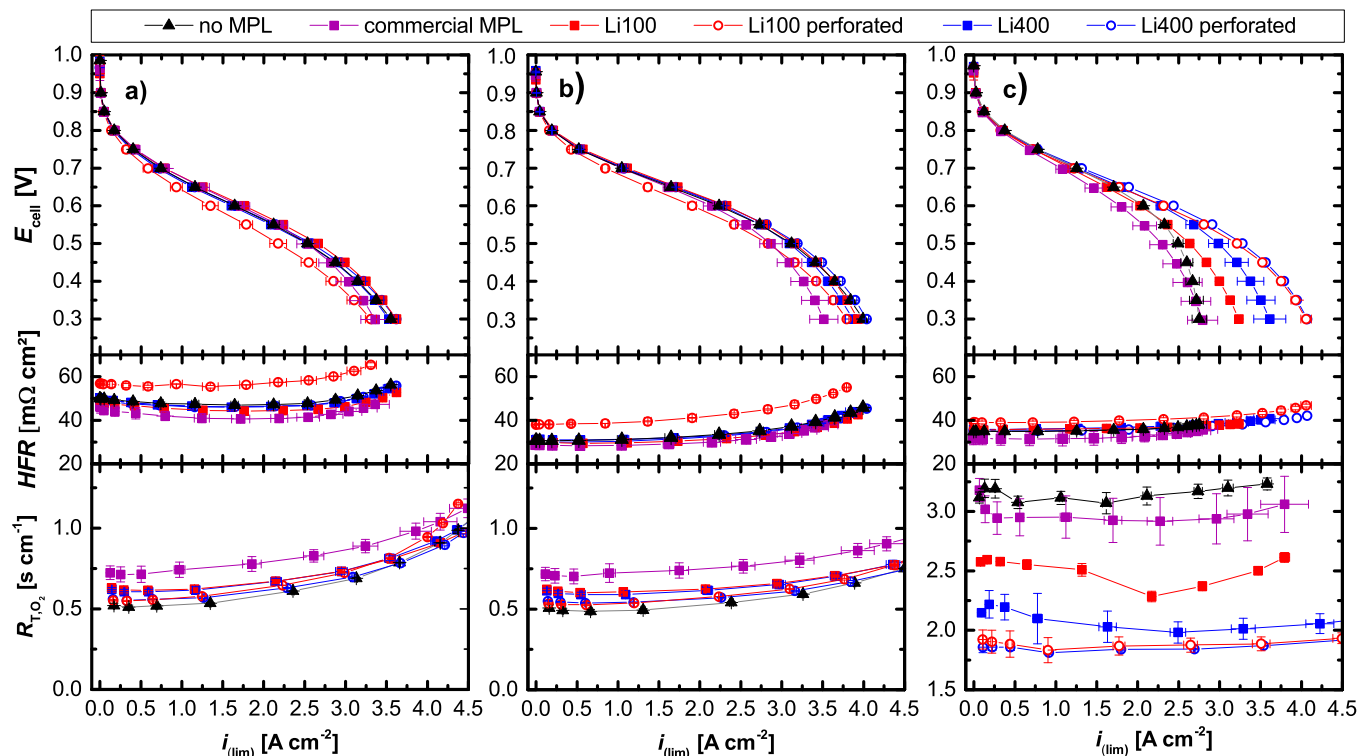
Figure 8. Differential-flow polarization curves showing cell voltage (E_{cell}, top) and high frequency resistance (HFR, middle) versus current density (i) as well as total oxygen transport resistance (R_{T,O_2}, bottom) versus the limiting current density (i_{lim}) for GDL-substrate with no MPL and the following MPLs coated on the same substrate: commercial MPL (Freudenberg), Li100 MPL, Li100 perforated MPL, Li400 MPL, Li400 perforated MPL. Operating conditions are (a) dry: $T_{cell} = 80°C$, $RH = 70\%$, $p_{abs} = 170$ kPa; (b) standard: $T_{cell} = 80°C$, $RH = 100\%$, $p_{abs} = 170$ kPa; and, (c) humid: $T_{cell} = 50°C$, $RH = 120\%$, $p_{abs} = 300$ kPa. The limiting current density is measured for various dry oxygen contents ($x_{O_2,dry}$) between 0.5% and 28%. The error bars represent the standard deviation of two independent measurements.

noted that the cell performance at the here chosen humid conditions is similar to that under standard and dry conditions, despite the impact of liquid water formation. This is mainly attributed to the higher pressure of 300 kPa compared to 170 kPa, which enhances the oxygen reduction kinetics (the decrease in the oxygen diffusion coefficient with increasing pressure is compensated by the higher oxygen partial pressure).

An interesting feature of the oxygen transport resistances shown in Figures 8a and 8b is that they increase at different degrees depending on the relative humidity as the limiting current density exceeds ≈1.5 A cm^{-2}, which in principle could be caused by the formation of liquid water within the MPL and/or the GDL-substrate.[26] However, if it were indeed caused by water condensation, the increase of R_{T,O_2} would be more pronounced at $RH = 100\%$ than at 70% RH. As our data show the opposite trend (from 1.5 to 4.5 A cm^{-2}, R_{T,O_2} increases by a factor of ≈1.6-2 at 70% RH and of ≈1.2-1.5 at 100% RH), the increase of R_{T,O_2} with current density is rather caused by an unfortunate shortcoming of the determination of R_{T,O_2} by the limiting current density method: as i_{lim} is measured at 0.05 V for $x_{O_2,dry}$ ≥ 12%, significant amounts of heat are released at elevated limiting current density, which can result in a significant increase of the MEA temperature (compared to the nominal flow field temperature) and a concomitant decrease of the local relative humidity at the MEA. This, in turn would lead to an increase of the ionic conduction resistance in the membrane, as is indeed apparent in the HFR data (see middle panels of Figures 8a and 8b) and therefore also in the electrodes. Under these circumstances, the current density distribution in the cathode electrode will be skewed toward the cathode/membrane interface,[43] leading to a higher local current density and thus to an increase in the non-Fickian transport resistance ($R_{O_2,cathode}$ and $R_{O_2,other}$ in Equation 2), ultimately reducing i_{lim} and thus increasing the calculated R_{T,O_2}.[44] The observation that this increase of R_{T,O_2} with increasing

current density is lower at 100% RH than at 70% RH clearly supports that it originates from membrane and electrode dry-out. On the other hand, for the over-humidified condition at low-temperature and high-pressure (Figure 8c), the R_{T,O_2} remains constant with current density, since the GDL is water-saturated at already low current densities and since the local temperature rise of the MEA (also indicated by the HFR increase) is not sufficient to remove liquid water and to dry-out the MEA.

At small limiting current densities, i.e., where R_{T,O_2} is constant, the above described dry-out effect is not relevant and this condition is best suited to evaluate the more subtle differences between the GDLs. Figure 9 shows R_{T,O_2} measured at comparable oxygen concentration gradients (i.e., at equal and low $x_{O_2,dry}$). As expected, under dry and standard conditions, the GDL-substrate without MPL (black bars) has the lowest R_{T,O_2}, as any MPL adds an additional transport barrier; the Li100 and Li400 MPLs (red and blue bars) show a small and similar increase in R_{T,O_2}, while the perforated MPLs (hatched bars) offer some direct diffusion pathways which leads to a reduced R_{T,O_2} compared to the non-perforated materials. The highest R_{T,O_2} is determined for the GDL with commercial MPL, which is due to the fact that it is ≈60% thicker. Under humid conditions, R_{T,O_2} increases by a large factor due to the higher operating pressure (300 kPa vs. 170 kPa) and due to water-saturation of the GDL. Here, the GDL-substrate without MPL now has the highest transport resistance, while the other GDLs follow the same trend as under dry and standard conditions.

To investigate the impact of the MPL on the dry-to-wet transition, Figure 10 shows R_{T,O_2} at $T_{cell} = 50°C$, $RH = 77\%$ and $p_{abs} = 400$ kPa, which is representing an under-humidified condition. The constant R_{T,O_2} level at ≲0.75 A cm^{-2} is showing the dry operation, where no water condensation is expected. With increasing i_{lim}, more water is produced until it starts to condense and to partially saturate the MPL/GDL-substrate and the electrode/MPL interface.
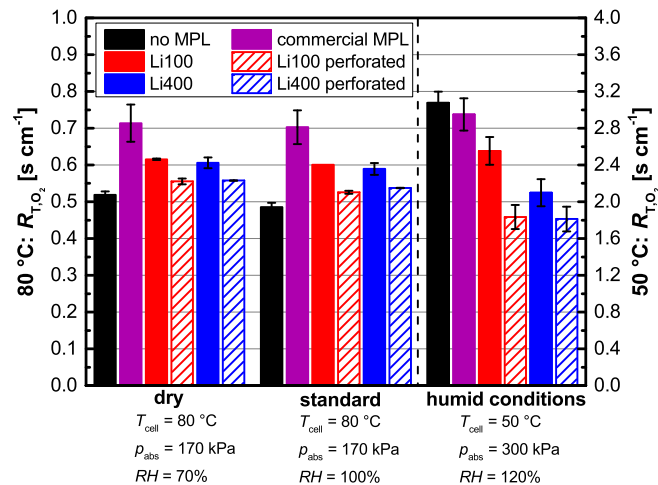
Figure 9. Total oxygen transport resistance (R_{T,O_2}) for GDL-substrate without MPL and the following MPLs coated on the same substrate at the three different operating conditions examined in Figure 8: commercial MPL (Freudenberg), Li100 MPL, Li100 perforated MPL, Li400 MPL, Li400 perforated MPL. R_{T,O_2} values are extracted from Figure 8 at $x_{O_2,dry} = 2\%$ for 80°C and $x_{O_2,dry} = 4\%$ for 50°C, which corresponds to the dry plateau region (for dry and standard conditions) and to the wet plateau region (for humid condition). Note that R_{T,O_2} at humid conditions is plotted on the right y-axis. The error bars represent the standard deviation of two independent measurements.

Figure 10. R_{T,O_2} as function of limiting current density for substrate with no MPL and the following MPLs coated on the same substrate: commercial MPL (Freudenberg), Li100 MPL, Li100 perforated MPL, Li400 MPL, Li400 perforated MPL. Operating conditions are $T_{cell} = 50°C$, $RH = 77\%$, $p_{abs} = 400$ kPa; i_{lim} was measured for various dry oxygen contents ($x_{O_2,dry}$) between 0.5% and 28%. The error bars represent the standard deviation of two independent measurements.

This leads to an increase in R_{T,O_2} until a maximum level of saturation is reached. From this point on, a roughly constant R_{T,O_2} at a high level is measured.[26,28] In the dry region, the same trends appear as for dry and standard conditions in Figures 8a and 8b and in Figure 9. The transition to a water-saturated diffusion medium is starting at a similar i_{lim} for all materials. In the wet region, i.e., at $\gtrsim 1.5$ A cm^{-2}, differences between the materials are clearly visible and follow the trend as under humid conditions in Figure 8c and in Figure 9.

Discussion

Oxygen transport in the dry region.—The presented results of the Li100 and Li400 MPLs reveal only a minor impact of the utilized carbon black and the resulting porous structure on the total oxygen transport through the respective dry GDLs in the absence of liquid water (i.e., in the so-called dry region). At $p_{abs} = 170$ kPa, their transport resistance is almost identical at dry (80°C/70% RH) and standard conditions (80°C/100% RH), with $R_{T,O_2} \approx 0.6$ s cm^{-1} (see left and middle panels in Figure 9). When subtracting the transport resistance of the uncoated GDL-substrate ($R_{T,O_2} \approx 0.5$ s cm^{-1}), the resulting transport resistance through the Li100 and Li400 MPLs is $R_{MPL,O_2} \approx 0.12 \pm 0.01$ s cm^{-1} (Li100 MPL) and $R_{MPL,O_2} \approx 0.10 \pm 0.03$ s cm^{-1} (Li400 MPL). As all tested Li100 and Li400 MPLs have the same thickness, the effective diffusion coefficient (inversely proportional to the pressure-dependent contribution of R_{O_2}) for both MPLs and thus the ratio of τ/ε (see Eq. 4) is essentially identical. However, the here used assumption that the MPL transport resistance can be considered a property which is entirely independent of the GDL-substrate is only a zero-order estimate for the Li100 and Li400 MPLs, as there clearly is a significant intrusion of these MPLs into the GDL-substrate (see Figures 7f and 7j). This is different for the commercial MPL (see Figure 7e), with its $\approx$2-fold higher oxygen transport resistance through the MPL of $R_{MPL,O_2} \approx 0.22 \pm 0.06$ s cm^{-1} under these conditions (based on $R_{T,O_2} \approx 0.71$ s cm^{-1}) which in consequence means that the different MPL/GDL-substrate interfaces (less intrusion for commercial MPL) and the only $\approx$1.6-fold higher thickness cannot entirely explain the 2-fold increase of R_{MPL,O_2}. The exclusively smaller pore sizes of the commercial MPL (see Figure 5) however can rationalize its higher diffusion resistance. The same trends can be observed at the higher pressure of $p_{abs} = 400$ kPa (Figure 10): subtracting the GDL-
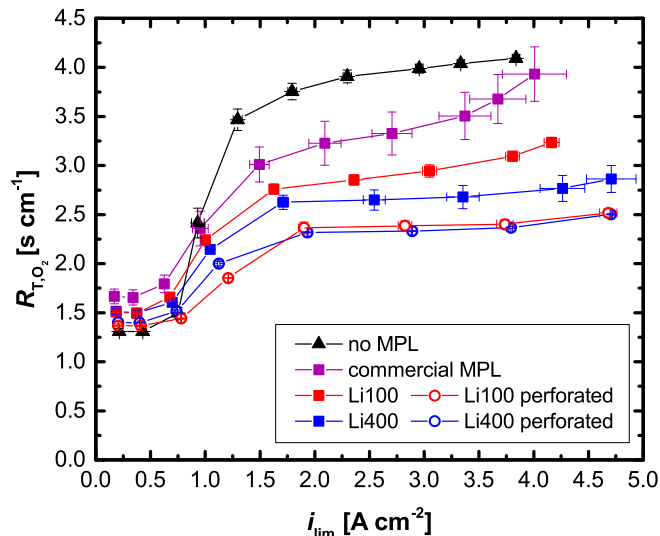
substrate transport resistance ($R_{T,O_2} \approx 1.31$ s cm^{-1}), oxygen transport resistance contribution from the commercial MPL ($R_{MPL,O_2} \approx 0.35 \pm 0.10$ s cm^{-1}) is $\approx$1.8-fold larger than that for the Li100 and Li400 MPLs ($R_{MPL,O_2} \approx 0.19 \pm 0.03$ s cm^{-1} and $R_{MPL,O_2} \approx 0.19 \pm 0.06$ s cm^{-1}).

In conclusion, while the total transport resistance of the various GDLs in the dry plateau region only varies by less than $\approx$30% (i.e., between the commercial MPL/GDL-substrate and the MPL-free GDL-substrate), reflected by the essentially identical differential-flow performance curves (see Figures 8a and 8b), the nominal contribution from the MPL (R_{MPL,O_2}) differs by a factor of $\approx$2. Further improvements in the MPL transport resistance in the dry plateau region, are observed with the perforation of the Li100 and Li400 MPLs: at $T_{cell} = 80°C$ and $p_{abs} = 170$ kPa, R_{MPL,O_2} amounts to $\approx 0.04 \pm 0.02$ s cm^{-1} (Li100 perforated MPL) and $\approx 0.05 \pm 0.01$ s cm^{-1} (Li400 perforated MPL; see left and middle panel of Figure 9) and at $T_{cell} = 50°C$ and $p_{abs} = 400$ kPa, R_{MPL,O_2} is $\approx 0.06 \pm 0.04$ s cm^{-1} (Li100 perforated MPL) and $\approx 0.09 \pm 0.03$ s cm^{-1} (Li400 MPL), showing that in both cases the large pores in the perforated MPLs (see Figures 7g and 7k) substantially enhance the oxygen transport. Since the MPL thickness remained the same and since the impact of the overall MPL void volume fraction is expected to be only minor (Li100 MPL: increase of ε from 79% to 86% would result in an 8% reduction of R_{MPL,O_2}; Li400 MPL: increase of ε from 68% to 77% results in a 12% reduction of R_{MPL,O_2}) this implies a much lower tortuosity τ for perforated MPLs (see Eq. 4), providing strong support to the presence of large pores/cracks extending across the MPL. However, these differences have almost no impact on the polarization curves under dry and standard conditions at a commonly used benchmark cell voltage of 0.6 V (see Figure 8), as the differences in total mass transport resistance are small.

Impact of carbon black type in non-perforated MPLs in the presence of liquid water.—In contrast to the above described performance in the dry region, the total oxygen transport resistance of the GDL at humid conditions, i.e, in the so called wet region where the GDL is partially water-filled, is significantly impacted by the MPL. This is also illustrated by the large differences in the fuel cell polarization curves (see Figure 8c), indicating different oxygen transport mechanisms in the presence of liquid water. It has been shown that

the MPL prevents the accumulation of liquid water in the porous structure of the substrate close to the cathode and that it also creates preferred water transport pathways, which reduces the water saturation level inside the substrate.[2,6,7] This effect is also observed in our data, where the substrate without MPL reveals the highest oxygen transport resistance due to severe water blockage in the GDL pores close to the electrode, while all MPLs show an improvement in terms of oxygen transport (lower panel of Figure 8c). Amongst the non-perforated carbon black based MPLs, the Li400 MPL exhibits the smallest R_{T,O_2} of ≈ 2.1 s cm^{-1}, followed by the Li100 MPL with ≈ 2.6 s cm^{-1}, and lastly by the commercial MPL with a much higher value of ≈ 3.9 s cm^{-1}.

First considering the here prepared non-perforated Li400 and Li100 MPLs, their different oxygen transport properties in the wet region could be explained by their different morphology, with the better performing Li400 MPL showing a larger maximum in its pore size distribution compared to the Li100 MPL (≈ 328 nm vs. ≈ 67 nm; see Figure 4, Figure 5, and Table II). Under the assumption that in the wet region liquid water will have to penetrate the MPL by an eruptive release mechanism of water from the cathode through the MPL (which means a continuous filling and emptying of pores with water), the Washburn equation (Eq. 1) would predict that larger pores in the MPL would facilitate liquid water transport and are thus preferred at these operating conditions. The smaller these hydrophobic pores on the other hand, the larger would be the extent of water retention and its accumulation at the cathode/MPL interface, thereby reduce the effective diffusion of oxygen. This would explain the lower oxygen transport resistance and the better performance of the Li400 vs. the Li100 MPL (see Figure 8c). At first glance inconsistent with this hypothesis is the fact that the Li100 MPL coated on the GDL-substrate also exhibits many larger pores with diameters between $\approx 0.1 - 10 \mu$m (see Figure 5) which should more easily facilitate liquid water transport. However, as none of these large pores in the micrometer range are observed in the top-view SEM images (see Figure 7e), we assume that these are internal pores, which can be recognized as small cracks in cross-sectional images (see Figure 7f). This means that liquid water still has to percolate through the small pores located at the surface of the MPL. This leaves the question why the commercial MPL with a similar maximum in the pore size distribution (≈ 64 nm; Figure 5) as the Li100 MPL displays a much higher R_{T,O_2} value and much worse fuel cell performance (Figure 8c). While part of it may be ascribed to its 60% larger thickness, it may also be related to differences in the MPL/GDL-substrate interface, which is very sharp for the commercial MPL and more intertwined for the Li100 MPL (compare Figures 7d and 7f), whereby the latter may be conductive to water transfer into the GDL-substrate.

Impact of MPL perforation in the presence of liquid water.—The perforation of MPLs creates a heterogeneous pore structure with a microporous framework defined by the carbon black (see Hg porosimetry in Figure 4) and by large micrometer-sized pores going all across the MPL which are produced by the pore former (see SEM images in Figure 7). Extending on the above discussion, such an MPL structure should facilitate the transport of liquid water through the large pores at very low capillary pressure, at which the small pores defined by the carbon black would remain water-free and thus serve as oxygen transport pathway. This proposed mechanism is illustrated in Figure 11, where the expected liquid water transport pathway through the MPL is shown by an SEM image of a perforated Li400 based MPL, visualizing our hypothesis that the large pores penetrating across the MPL are preferentially filled with liquid water, while the small pores defined by the carbon black structure remain water-free, enabling efficient oxygen transport without an additional transport barrier.

As one would expect based on this hypothesis, the experimental data clearly show that the oxygen transport resistance in the wet plateau region is indeed substantially lower for the perforated MPLs compared to the non-perforated MPLs (see Figure 10). Under conditions where liquid water is present in the GDL, the perforation reduces R_{T,O_2} by $\approx 25\%$ for the Li100 MPL and by $\approx 14\%$ for the
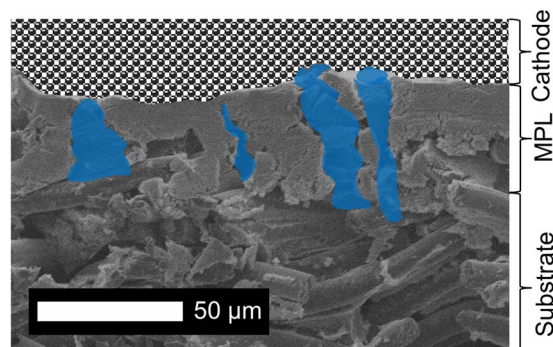

Figure 11. Illustration of the proposed liquid water transport mechanism through perforated MPLs from the cathode electrode (upper hatched region) toward the GDL-substrate, using an SEM image for a perforated Li400 MPL. Large pores caused by the pore former are hypothesized to allow the effective transport of liquid water (blue colored region) while most regions of the MPL are free of liquid water and thus available for efficient oxygen gas transport.

Li400 MPL at both $T_{cell} = 50°C$, $RH = 120\%$ and $p_{abs} = 300$ kPa and $T_{cell} = 50°C$, $RH = 77\%$ and $p_{abs} = 400$ kPa (see right panel of Figure 9 and Figure 10). This impacts also the polarization curves, where in Figure 8c the perforated MPLs show the highest performance with 2.3 A cm^{-2} (Li100 perforated) and 2.4 A cm^{-2} (Li400 perforated) at 0.6 V as well as the highest limiting current densities. A particularly interesting feature of the perforated MPLs under these humid conditions is that their oxygen transport resistance (lower panel of Figure 8c) is essentially identical ($R_{T,O_2} \approx 1.8$ s cm^{-1}), even though both MPLs without perforation show very different R_{T,O_2} (≈ 2.6 s cm^{-1} for the Li100 MPL vs. 2.1 s cm^{-1} for the Li400 MPL). The same behavior is even more clearly illustrated in Figure 10, where due to the higher pressure and the lower relative humidity the dry-to-wet plateau transition can be followed. At small current densities (i.e., in the dry plateau region), the non-perforated Li100/Li400 MPLs show the same R_{T,O_2} (≈ 1.5 s cm^{-1}) and their perforated versions the same slightly smaller R_{T,O_2} (≈ 1.4 s cm^{-1}). The start of water condensation is observed at ≈ 0.75 A cm^{-2} for all GDLs, which is indicated by a rapid increase of R_{T,O_2}. A state of high water saturation is reached for all materials at ≈ 1.5 A cm^{-2}. From this point on, a further more gradual increase of R_{T,O_2} for the Li100 and the commercial MPL suggests a continuous accumulation of water at an already high saturation level, while R_{T,O_2} for the Li400 and the perforated MPLs remain at an essentially constant level. Analogous to the humid condition at 300 kPa and $RH = 120\%$ (lower panel, Figure 8c) where the wet plateau region is established already at the lowest current density, different R_{T,O_2} values are observed for the non-perforated Li100/Li400 MPLs, while both perforated MPLs end up at the same R_{T,O_2} value. This actually confirms our above hypothesis that there exist two transport pathways in the perforated MPLs, namely transport of liquid water in the large pores at low capillary pressure while oxygen is transported in the small micropores within the non-cracked MPL segments which remain water-free at low capillary pressure (see Figure 11): in this case, the identical dry plateau oxygen transport resistance for the non-perforated Li100 and Li400 MPLs would predict the observed identical R_{T,O_2} in the wet plateau for the perforated MPLs. Similarly, in case of the non-perforated Li100 and Li400 MPLs, where oxygen and liquid water have to share pores of similar size as transport pathways, the MPL with the larger pore size distribution maximum (≈ 328 nm for Li400 vs. ≈ 67 nm for Li100) should have a lower R_{T,O_2} in the wet plateau region, exactly as observed in Figure 8c and Figure 10. These observations, we believe, provide rather strong evidence for the transport mechanisms in perforated (or cracked) MPLs which are illustrated in Figure 11.

These results are also in agreement with studies from Lu et al.,[18] Gerteisen et al.,[16] Kong et al.[22] and Selvarani et al.[32] For laser

perforated MPLs[18] or GDLs,[16] significant improvements in limiting current density were measured at humid conditions (i.e., at low cell temperatures of $T_{cell} = 55°C$[16] and $T_{cell} = 40°C$[16]). Also for MPLs, which are perforated by using pore-forming agents, significant performance enhancements are observed in oxygen or air at 60°C[32] and 75°C[22] and fully humidified gases with a maximum performance for an optimum pore former content. But we do not agree with the explanation of Kong et al. for this observation, who argue with the effect of capillary condensation in sub-nanometer size pores, which, however, are not relevant for gas transport through the layer, and their assumption that oxygen transport is realized in large dry pores. Thus, they completely neglect the more likely capillary effect, which is also suggested by other studies and would result in oxygen transport in smaller pores, while liquid transport is occurring in the larger pores.[10,14,19] On the contrary, Owejan et al. found no impact of intentionally introduced cracks in the MPL on the fuel cell performance at both dry ($T_{cell} = 80°C$, $p_{abs} = 150$ kPa and $RH = 66\%$) and humid conditions ($T_{cell} = 60°C$, $p_{abs} = 270$ kPa and $RH = 100\%$).[2] The authors conclude that even at humid conditions water vapor transport is sufficient to remove product water from the electrode through the MPL. From the SEM cross-sectional images one can estimate that the average distance between the cracks is ca. 200 µm compared to ca. 50 µm in the present study (compare Figure 2 in Ref. 2 to Figures 7h and 7l in this study). It is unclear whether the crack density in the study by Owejan et al. was sufficient to allow for the here proposed bi-functional transport pathways (see Figure 11). Based on geometric arguments, effective dual transport pathways would require distances between cracks which are on the order of the electrode thickness (≈10 µm), and average crack distances of >100 µm are probably not effective, which might be the origin of the discrepancy between their and our findings.

An alternative explanation for the observed phenomena in the present study could be a change of the temperature distribution inside the MEA with different MPL materials. Previous studies have shown that the MPL type, thickness, and its intrusion into the substrate affect its thermal conductivity and thus influence the temperature gradient between the electrode and the GDL-substrate.[45–48] The lower the thermal conductivity of the MPL, the higher is this temperature gradient, which enables a larger fraction of liquid water to be transported by vapor phase diffusion, presumably reducing the liquid water fraction inside the porous layers and reducing oxygen transport resistances. For the same MPL composition, the thermal conductivity should obviously decrease with increasing porosity, so that a larger thermal gradient and thus improved oxygen transport would be predicted for perforated MPLs on this basis, which is indicated by the reduced R_{T,O_2} in our measurements.

However, based on this thesis, a larger thermal gradient would also cause a smaller membrane hydration at high current densities due to a decreased local RH,[45,49] which should manifest itself in a larger increase of the HFR for the perforated MPLs at elevated current densities, in particular at dry conditions. This is not the case as can be seen in Figure 8a. Furthermore, assuming a similar bulk thermal conductivity of the two utilized acetylene black based MPLs (same PTFE content) would also suggest, that the Li100 MPL ($\varepsilon = 79\%$) should show a smaller R_{T,O_2} compared to the Li400 MPL ($\varepsilon = 68\%$) due to its higher porosity, which again is not supported by our measured oxygen transport resistances (see Figure 8c, Figure 9, and Figure 10). Finally, small MPL thermal conductivity differences would also likely be minimized by the presence of high water contents, which significantly increase the overall thermal conductivity of porous media.[50] From these observations, we conclude that the oxygen transport resistance differences between our different MPLs are not related to MPL thermal conductivity differences, but are mostly caused by an efficient liquid water transport as stated before.

Thus, based on our data and analysis, a bi-functional pore network is able to facilitate liquid water transport through the MPL and to reduce the oxygen transport resistance at humid conditions (i.e., in the wet plateau region). As water in these structures is transported primarily through the large pores, the total oxygen mass transport resistance
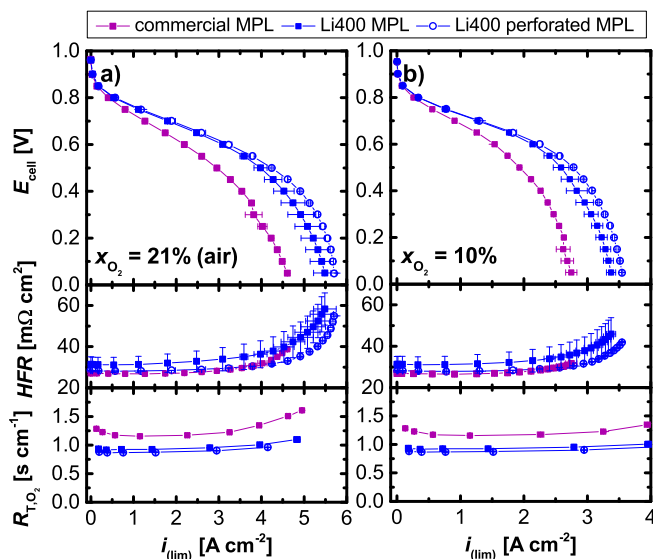

Figure 12. Cell voltage (E_{cell}, top) and high frequency resistance (HFR, middle) vs. current density (i) and total oxygen transport resistance (R_{T,O_2}, bottom) vs. the limiting current density for GDL-substrate coated with the following MPLs: commercial MPL (Freudenberg), Li400 MPL, and Li400 perforated MPL. Operating conditions are: (a) $T_{cell} = 80°C$, $RH = 100\%$, $p_{abs} = 300$ kPa, with cathode feed air ($x_{O_2,dry} = 21\%$); (b) $T_{cell} = 80°C$, $RH = 100\%$, $p_{abs} = 300$ kPa, with cathode feed $x_{O_2,dry} = 10\%$ in N_2. Limiting current densities (i_{lim}) are measured for various dry oxygen contents ($x_{O_2,dry}$) between 0.5% and 24%. The error bars represent the standard deviation of two independent measurements.

becomes largely independent from the pore size distribution within the solid part of the MPL (defined by the carbon black structure), as long as the oxygen transport resistance through the MPL in the dry plateau region is comparable. This provides a new design strategy for MPLs: while the "ideal" MPL would exhibit independent arrays of hydrophilic and hydrophobic pores/regions (as, e.g., demonstrated for GDL-substrates by Forner-Cuenca et al.[51]), an alternative approach shown here is to create a bi-modal pore size distribution of small and large pores, both with hydrophobic properties. In general, the here presented approach of applying a pore former polymer to produce such a bi-functional porous network is in principal cost-efficient and applicable to a large-scale production. Despite these advantages, this strategy also raises some critical questions toward the practicality in a fuel cell. The MPL perforation leads to an inhomogeneous surface, which could cause localized resistance variations (as indicated by the increased HFR of the perforated Li100 MPL), but could also affect the heat transfer and result in local hot-spots. Furthermore, the CCM is mechanically less stabilized if the perforations are too large. These thermal and mechanical stresses might lead to local degradation phenomena over extended operating times, which certainly needs to be evaluated before an actual application of perforated MPLs.

Impact of pressure and oxygen concentration on the MPL Performance.—Although the here prepared GDLs show advantages under humid conditions ($T_{cell} = 50°C$, $RH = 120\%$, $p_{abs} = 300$ kPa), it is somewhat disappointing that no benefits are observed under standard operating conditions ($T_{cell} = 80°C$, $RH = 100\%$, $p_{abs} = 170$ kPa) at which the GDL water saturation level is low (compare Figures 8a and 8b with 8c). However, in the recent years, in order to reach a high efficiency (cell voltage of >0.6 V) of the fuel cell system at high current densities (>2 A cm^{-2}), higher operating pressures are being considered for automotive fuel cell systems.[44] Here, a trade-off between the higher air compressor power requirement and the fuel cell power improvement has to be considered. To evaluate the performance gains at high pressure, differential-flow polarization curves at $T_{cell} = 80°C$, $RH = 100\%$ and $p_{abs} = 300$ kPa are recorded for the

commercial MPL, the Li400 MPL and the Li400 perforated MPL. Two different oxygen contents of 21% of O_2 in N_2 and 10% of O_2 in N_2 simulate the concentrations at the cell air inlet and its outlet at an assumed cathode stoichiometry of $\approx$1.75. The results are shown in Figure 12.

Due to a doubling of oxygen partial pressure at $p_{abs} = 300$ kPa (Figure 12a), the oxygen reduction kinetics are significantly enhanced compared to $p_{abs} = 170$ kPa (Figure 8b). This effect causes higher voltages in the kinetically dominated region, indicated by the cell voltages obtained at 1 A cm^{-2} of 0.77 V (Li400 and perforated Li400 MPLs) or 0.73 V (commercial MPL) at 300 kPa compared to 0.71 V at 170 kPa for these three GDLs. While at 170 kPa (Figure 8b) the differences between the three GDLs are marginal at 0.6 V, significant improvements by the advanced MPL materials are observed at 300 kPa. At 21% O_2 (Figure 12a), the commercial MPL exhibits 2.2 A cm^{-2}, the Li400 MPL 3.1 A cm^{-2}, and the Li400 perforated MPL 3.2 A cm^{-2}; at 10% O_2 (Figure 12b), analogously high improvements are observed (1.5 A cm^{-2} for the commercial MPL vs. 2.1 A cm^{-2} for the Li400 MPL and 2.2 A cm^{-2} for the perforated Li400 MPL). This corresponds to a total performance improvement of $\approx$45% for both air and 10% O_2, and thus to a reduction of the platinum specific power density at 0.6 V of $\approx$30% from $\approx$0.38 g$_{Pt}$/kW for the commercial MPL/GDL-substrate to $\approx$0.26 g$_{Pt}$/kW for the perforated Li400 MPL. While $\approx$0.26 g$_{Pt}$/kW are still quite a bit off from the DoE target of $\leq$0.1 g$_{Pt}$/kW, preliminary data have already shown that combination of advanced MEAs (thinner membranes and lower Pt loadings) with sophisticated MPL materials very closely approach the DoE target under these high-pressure conditions.

As a last step, we want to examine the origin of the observed large fuel cell performance improvement of the Li400 MPL and the perforated Li400 MPL with fully-humidified reactants at 300 kPa (Figure 12) compared to the minor differences at 170 kPa (Figure 8b), namely whether this is due to improved liquid water transport (as clearly is the case at the humid conditions shown in Figure 8c) or whether it is due to the enhanced oxygen transport in the absence of water saturation. This is not a priori obvious, since the binary diffusion coefficient of water vapor in the oxygen/nitrogen/vapor gas mixture (M) decreases with $D_{H_2O|M} \sim p_{abs}^{-1}$, and the resulting slower water vapor transport was shown lead to water condensation, i.e., to a shift of the dry-to-wet-plateau transition to lower current densities.[26]

In general, the effect of pressure on the total oxygen transport resistance is different for the different terms in Equation 2. The pressure independent contribution to the total oxygen transport, R_{PI,O_2}, is caused by Knudsen diffusion resistances in small pores (mainly in the catalyst layer) and a resistance attributed to the Pt surface or the ionomer film, which is dependent on the electrode roughness factor.[24,44] Raising the operating pressure, this term stays constant as the oxygen partial pressure gradient from flow field to the catalyst surface during operation is increased[24,26] and for a similar cathode electrode, it was determined as $R_{PI,O_2} \approx 0.15$ s cm^{-1} (at 80°C for 0.4 mg$_{Pt}$ cm^{-2}).[24] On the other hand, the pressure dependent part (R_{PD,O_2}) is proportional to the total pressure: $R_{PD,O_2} \sim D_{O_2|M}^{-1} \sim p_{abs}$,[26] where $D_{O_2|M}$ represents the binary diffusion coefficient of oxygen in the oxygen/nitrogen/vapor gas mixture (M). Hence the performance effect of the oxygen pressure gradient increase is almost cancelled out by the increase of transport resistance. Based on the R_{T,O_2} from Figure 8b at 170 kPa, we can estimate the R_{T,O_2} at 300 kPa with Equation 10.

$$R_{T,O_2(p_2)} = \left(R_{T,O_2(p_1)} - R_{PI,O_2}\right) \cdot \frac{p_2}{p_1} + R_{PI,O_2} \qquad [10]$$

With $R_{PI,O_2} \approx 0.15$ s cm^{-1} (see above), R_{T,O_2} is expected to increase from 0.59 s cm^{-1} at 170 kPa (from Figure 8b) to 0.93 s cm^{-1} at 300 kPa for the Li400 MPL, from 0.54 s cm^{-1} at 170 kPa (from Figure 8b) to 0.87 s cm^{-1} at 300 kPa for the perforated Li400 MPL, and from 0.70 s cm^{-1} at 170 kPa (from Figure 8b) to 1.12 s cm^{-1} at 300 kPa for the commercial MPL. This is in quite excellent agreement with the measured values shown in Figure 12 (0.92 s cm^{-1} for Li400, 0.87 s cm^{-1} for Li400 perforated, and 1.17 s cm^{-1} for commercial MPL/GDL). As it has already been shown that no liquid water is

present in the MPL/GDL-substrate under the standard conditions of Figure 8b ($T_{cell} = 80$°C, $RH = 100$%, $p_{abs} = 170$ kPa) and as our above calculation does not include the additional oxygen transport resistance which would be present under conditions where the GDL is saturated with liquid water, we can conclude from the agreement between measured and calculated R_{T,O_2} values that also at the conditions of Figure 12 ($T_{cell} = 80$°C, $RH = 100$%, $p_{abs} = 300$ kPa) no significant amount of liquid saturation occurs in the GDL.

Nevertheless, in the polarization curves with air and 10% O_2 at 300 kPa (Figure 12), mass transport effects obviously become significant at relevant voltages >0.6 V, leading to a very different performance of the various GDLs, in strong contrast to the 170 kPa polarization curves (Figure 8b). Due to accelerated ORR kinetics, current densities between 2.2 A cm^{-2} and 3.2 A cm^{-2} are reached at 0.6 V. Because the mass transport overpotential is a function of the current density, larger differences in the performance are detected at 300 kPa compared to 170 kPa. When simulating the stack outlet conditions with supplying 10% O_2 in N_2 to the cathode, the limiting current density is decreasing by a similar ratio compared to air as expected from the decrease in oxygen concentration. From Equation 3, one would expect a ratio between the air and 10% O_2 condition of 21/10 = 2.1 assuming a constant R_{T,O_2} independent of the limiting current density. In reality, however, we measure a smaller ratio of 1.6–1.7 (depending on GDL), which we attribute to the increasing R_{T,O_2} at elevated $i_{lim} > 4$ A cm^{-2} as explained in the previous discussion. The better performance for the Li400 perforated MPL shows that also at smaller oxygen partial pressure gradients, the MPL still exhibits a major role. Hence, for high pressure operation and standard temperature and RH (80°C and 100% RH), sophisticated MPLs are necessary, which feature a high diffusivity (i.e. high ε/τ) for oxygen in order to protract the beginning of the oxygen transport limited region and to reach high current densities, even though only minor amounts of liquid water are present. At the same time, robust MPLs/GDLs have to be able to effectively transport both oxygen and liquid water under conditions where significant amounts of water saturation in the GDL occur.

Conclusions

In this paper we present fuel cell data and characterization for two MPLs with different carbon blacks and a commercial MPL. We observe that the MPL pore structure has significant influence on the oxygen transport, in particular at conditions of high liquid water saturation. The results at $T_{cell} = 50$°C, $RH = 120$%, $p_{abs} = 300$ kPa show a 15% smaller total oxygen transport resistance and better performance for the MPL with large pores (maximum 328 nm) than for the MPL with smaller pores (maximum 67 nm), while the performance at dry conditions ($T_{cell} = 80$°C, $RH = 70$%, $p_{abs} = 170$ kPa) is almost identical for both materials. This is explained by a reduced capillary pressure for larger hydrophobic pores which facilitates the transport of liquid water and prevents a blockage of oxygen transport pathways, while the oxygen transport in dry GDLs is unaffected.

Furthermore we present an approach to introduce large pores and cracks into the MPL by using a thermally decomposable pore former polymer. Our measurements suggest that these perforations create preferred transport pathways for liquid water, which reduce the oxygen transport resistance compared to the conventional carbon black based MPLs at humid operating conditions. From our results we can conclude that the transport of oxygen and water proceeds via separate pores of different size, which reduces the accumulation of liquid water at the MPL/cathode interface. Also at high pressure and normal conditions ($T_{cell} = 80$°C, $RH = 100$%, $p_{abs} = 300$ kPa), the newly developed MPLs exhibit advantages in performance due to the better diffusivity of oxygen through their structure, even though no significant amounts of liquid water are expected.

Summarized, with the present strategy the fuel cell performance at 0.6 V and humid conditions ($T_{cell} = 50$°C, $RH = 120$%, $p_{abs} = 300$ kPa) is improved by variation of the carbon black and by perforation via the reduction of the total oxygen transport resistance (R_{T,O_2}). Furthermore at elevated operating

pressure ($T_{cell} = 80°C$, $RH = 100\%$, $p_{abs} = 300$ kPa), we observe a significant impact of the MPL structural properties on the performance at a typical fuel cell operating temperature of 80°C, at which the perforated MPL exhibits a 45% higher current density than the commercial reference MPL.

List of Symbols

Variable	Unit	Description
A	cm^2	area
D_{eff}	m^2 s^{-1}	effective diffusion coefficient
$D_{O_2|M}$	m^2 s^{-1}	diffusion coefficient of oxygen in a gas mixture
d_{MPL}	μm	MPL thickness
$d_{particle}$	μm	particle diameter
d_{pore}	μm	pore diameter
E_{cell}	V	cell voltage
HFR	Ω cm^2	high frequency resistance
i	A cm^{-2}	current density normalized to geometric electrode area
i_{lim}	A cm^{-2}	limiting current density normalized to geometric electrode area
m	g	mass
p_{abs}	kPa	absolute pressure
p_c	kPa	capillary pressure
p_{H_2O}	kPa	partial pressure of water (at cell inlet)
$q_{vol.}$	%	volume fraction
R_{T,O_2}	s cm^{-1}	total oxygen transport resistance
R_{x,O_2}	s cm^{-1}	oxygen transport resistance of the component (x = GDL, MPL, flow field, cathode) or mechanism (x = PI (pressure independent), PD (pressure dependent))
RH	%	relative humidity
s	-	Reactant stoichiometry
T_{cell}	°C	fuel cell temperature
T_{sample}	°C	sample temperature
V	ml	volume
w	wt.%	mass fraction
$x_{O_2,dry}$	%	dry mole fraction of oxygen

Constant	Value	Unit	Description
F	96485	C mol^{-1}	Faraday constant
R	8.3145	J mol^{-1} K^{-1}	ideal gas constant

Greek	Unit	Description
γ_{H_2O}	N m^{-1}	surface tension of water
γ_{Hg}	N m^{-1}	surface tension of mercury porosity
ε	%	
θ	°	contact angle
ρ	g cm^{-3}	density
τ	-	tortuosity
ϕ_{PMMA}	vol.%	PMMA volume fraction

References

1. M. F. Mathias, J. Roth, J. Fleming, and W. Lehnert, in *Handbook of Fuel Cells*, W. Vielstich, H. A. Gasteiger, and A. Lamm, Editors, John Wiley & Sons, Ltd (2010).
2. J. P. Owejan, J. E. Owejan, W. B. Gu, T. A. Trabold, T. W. Tighe, and M. F. Mathias, *J. Electrochem. Soc.*, **157**, B1456 (2010).
3. J. M. Morgan and R. Datta, *J. Power Sources*, **251**, 269 (2014).
4. S. Park, J.-W. Lee, and B. N. Popov, *J. Power Sources*, **177**, 457 (2008).
5. S. Park, J.-W. Lee, and B. N. Popov, *J. Power Sources*, **163**, 357 (2006).
6. J. T. Gostick, M. A. Ioannidis, M. W. Fowler, and M. D. Pritzker, *Electrochem. Commun.*, **11**, 576 (2009).
7. P. Deevanhxay, T. Sasabe, S. Tsushima, and S. Hirai, *Electrochem. Commun.*, **34**, 239 (2013).
8. J. Lee, R. Yip, P. Antonacci, N. Ge, T. Kotaka, Y. Tabuchi, and A. Bazylak, *J. Electrochem. Soc.*, **162**, F669 (2015).
9. Y. Ji, G. Luo, and C.-Y. Wang, *J. Electrochem. Soc.*, **157**, B1753 (2010).
10. P. Deevanhxay, T. Sasabe, S. Tsushima, and S. Hirai, *J. Power Sources*, **230**, 38 (2013).
11. S. Prass, S. Hasanpour, P. K. Sow, A. B. Phillion, and W. Mérida, *J. Power Sources*, **319**, 82 (2016).
12. T. Sasabe, P. Deevanhxay, S. Tsushima, and S. Hirai, *Electrochem. Commun.*, **13**, 638 (2011).
13. R. Alink, J. Haussmann, H. Markotter, M. Schwager, I. Manke, and D. Gerteisen, *J. Power Sources*, **233**, 358 (2013).
14. S. S. Alrwashdeh, H. Markötter, J. Haußmann, T. Arlt, M. Klages, J. Scholta, J. Banhart, and I. Manke, *Energy*, **102**, 161 (2016).
15. J. Haußmann, H. Markötter, R. Alink, A. Bauder, K. Dittmann, I. Manke, and J. Scholta, *J. Power Sources*, **239**, 611 (2013).
16. D. Gerteisen, T. Heilmann, and C. Ziegler, *J. Power Sources*, **177**, 348 (2008).
17. Z. Lu and J. Waldecker, "Microporous layer structures and gas diffusion layer assemblies in proton exchange membrane fuel cells", *United States Pat. US 8,945,790 B2*, (issued: Feb. 3, 2015).
18. Z. Lu, J. Waldecker, M. Tam, and M. Cimenti, *ECS Transactions*, **69**, 1341 (2015).
19. H. Markötter, J. Haussmann, R. Alink, C. Totzke, T. Arlt, M. Klages, H. Riesemeier, J. Scholta, D. Gerteisen, J. Banhart, and I. Manke, *Electrochem. Commun.*, **34**, 22 (2013).
20. M. P. Manahan, M. C. Hatzell, E. C. Kumbur, and M. M. Mench, *J. Power Sources*, **196**, 5573 (2011).
21. M. P. Manahan and M. M. Mench, *J. Electrochem. Soc.*, **159**, F322 (2012).
22. C. S. Kong, D.-Y. Kim, H.-K. Lee, Y.-G. Shul, and T.-H. Lee, *J. Power Sources*, **108**, 185 (2002).
23. E. Gauthier, Q. Duan, T. Hellstern, and J. Benziger, *Fuel Cells*, **12**, 835 (2012).
24. D. R. Baker, D. A. Caulk, K. C. Neyerlin, and M. W. Murphy, *J. Electrochem. Soc.*, **156**, B991 (2009).
25. D. R. Baker, C. Wieser, K. C. Neyerlin, and M. W. Murphy, *ECS Transactions*, **3**, 989 (2006).
26. D. A. Caulk and D. R. Baker, *J. Electrochem. Soc.*, **157**, B1237 (2010).
27. H. Oh, Y. i. Lee, G. Lee, K. Min, and J. S. Yi, *J. Power Sources*, **345**, 67 (2017).
28. J. P. Owejan, T. A. Trabold, and M. M. Mench, *Int. J. Heat Mass Transfer*, **71**, 585 (2014).
29. B. Tjaden, S. J. Cooper, D. J. L. Brett, D. Kramer, and P. R. Shearing, *Current Opinion in Chemical Engineering*, **12**, 44 (2016).
30. D. A. G. Bruggeman, *Annalen der Physik*, **416**, 636 (1935).
31. J. Landesfeind, J. Hattendorff, A. Ehrl, W. A. Wall, and H. A. Gasteiger, *J. Electrochem. Soc.*, **163**, A1373 (2016).
32. G. Selvarani, A. K. Sahu, P. Sridhar, S. Pitchumani, and A. K. Shukla, *J. Appl. Electrochem.*, **38**, 357 (2008).
33. L. R. Jordan, A. K. Shukla, T. Behrsing, N. R. Avery, B. C. Muddle, and M. Forsyth, *J. Appl. Electrochem.*, **30**, 641 (2000).
34. L. R. Jordan, A. K. Shukla, T. Behrsing, N. R. Avery, B. C. Muddle, and M. Forsyth, *J. Power Sources*, **86**, 250 (2000).
35. E. Passalacqua, G. Squadrito, F. Lufrano, A. Patti, and L. Giorgi, *J. Appl. Electrochem.*, **31**, 449 (2001).
36. E. Antolini, R. R. Passos, and E. A. Ticianelli, *J. Power Sources*, **109**, 477 (2002).
37. X. L. Wang, H. M. Zhang, J. L. Zhang, H. F. Xu, Z. Q. Tian, J. Chen, H. X. Zhong, Y. M. Liang, and B. L. Yi, *Electrochim. Acta*, **51**, 4909 (2006).
38. G. Y. Gor, M. Thommes, K. A. Cychosz, and A. V. Neimark, *Carbon*, **50**, 1583 (2012).
39. A. V. Neimark, Y. Lin, P. I. Ravikovitch, and M. Thommes, *Carbon*, **47**, 1617 (2009).
40. C. Simon, F. Hasché, D. Müller, and H. A. Gasteiger, *ECS Transactions*, **69**, 1293 (2015).
41. C. Simon, F. Hasché, and H. A. Gasteiger, *J. Electrochem. Soc.*, **164**, F591 (2017).
42. H. Beyer, S. Meini, N. Tsiouvaras, M. Piana, and H. A. Gasteiger, *PCCP*, **15**, 11025 (2013).
43. K. C. Neyerlin, W. Gu, J. Jorne, A. Clark, and H. A. Gasteiger, *J. Electrochem. Soc.*, **154**, B279 (2007).
44. A. Kongkanand and M. F. Mathias, *The Journal of Physical Chemistry Letters*, **7**, 1127 (2016).
45. P. Antonacci, S. Chevalier, J. Lee, N. Ge, J. Hinebaugh, Y. Rip, Y. Tabuchi, T. Kotaka, and A. Bazylak, *Electrochim. Acta*, **188**, 888 (2016).

46. O. S. Burheim, H. Su, S. Pasupathi, J. G. Pharoah, and B. G. Pollet, *Int. J. Hydrogen Energy*, **38**, 8437 (2013).
47. R. Bock, A. Shum, T. Khoza, F. Seland, N. Hussain, I. V. Zenyuk, and O. S. Burheim, *ECS Transactions*, **75**, 189 (2016).
48. Y. A. Gandomi, M. D. Edmundson, F. C. Busby, and M. M. Mench, *J. Electrochem. Soc.*, **163**, F933 (2016).
49. C. K. Mittelsteadt and H. Liu, in *Handbook of Fuel Cells*, W. Vielstich, A. Lamm, and H. A. Gasteiger, Editors, John Wiley & Sons, Ltd (2010).
50. O. S. Burheim, G. Ellila, J. D. Fairweather, A. Labouriau, S. Kjelstrup, and J. G. Pharoah, *J. Power Sources*, **221**, 356 (2013).
51. A. Forner-Cuenca, J. Biesdorf, A. Lamibrac, V. Manzi-Orezzoli, F. N. Büchi, L. Gubler, T. J. Schmidt, and P. Boillat, *J. Electrochem. Soc.*, **163**, F1038 (2016).